Master's Thesis

A Study of the Field Distribution on Finite Array Endfire Antennas

by

Ellinor Persson
and
Ahmed Almuqayad

Department of Electrical and Information Technology
Faculty of Engineering, LTH, Lund University
SE-221 00 Lund, Sweden

Abstract

An endfire antenna is an array built up by smaller antennas, and is designed to direct the radiated power along the structure. In this thesis, we look at a very simple form, consisting of equally spaced monopoles over a perfectly conducting ground plane. After defining a unit cell, we set out to investigate whether a periodic structure model can be applied and used to calculate the electric field distribution on the antenna. The work is an initial study for a future research project on developing a more efficient algorithm for simulating very large array antennas.

Hypotheses are tested in an iterative manner. It is concluded that the field distribution differs from the one on a passive periodic structure, and a correction is proposed. The correction gives a better fit, but is not enough to pick up all variations. Remaining problems are the dependence on the number of elements in the array and to find a way to calculate the coefficients of the correction in advance. Also, the hypothesis that the propagation constant is real could not be falsified with the method used.

Acknowledgments

First of all we would like to express our appreciation to our supervisor Daniel Sjöberg for his support and guidance when working with this project. We would also like to thank Samuel Butler, Madeleine Kildal Schillinger, Daniel Hamngren, Joel Andersson and Andreas Tågerud for proofreading and for giving us many valuable comments during the writing of this report.

Ellinor Persson and Ahmed Almuqayad

Table of Contents

1

1 Introduction

1.1 Background and motivation

Periodic structures are used as a model in the most varied fields of science, from describing the crystal structure of a material [24] to microwave filters [2] used to filter out the accurate signals from the surrounding when using Bluetooth on your cell phone. An example from optics is the diffraction grating, for example a glass plate with periodically varying thickness. An incident wave propagating through the plate will bend with an angle that depends on the wavelength, and the grating can thus be used to separate different frequencies in a spectrum analyser [27].

In a group antenna, a number of antenna elements are placed close to each other in order to obtain a directional antenna with wide bandwidth. One example of a group antenna is the Yagi-Uda dipole array, consisting of dipole elements of different lengths and spacing of which one is driven and the other is parasitic. Yagi-Uda antennas are used in particular as home TV antennas. For TV-reception in fringe areas, log-periodic dipole arrays, where all elements are driven since they are electrically connected together, are used [9]. A Frequency Selective Surface (FSS) array is a periodic array of metallic patches. These types of arrays are used for example in radar and satellite communications [28].

While many theoretical models assume infinite extension of the structure, going from an infinite to a finite periodic structure gives rise to new phenomena that requires attention. In reality, all structures are finite, and therefore it is of great interest to find methods to handle these. The theory of finite periodic structures has been discussed for example by Ben A. Munk in his book "*Finite Antenna Arrays and FFS*" [23], and size requirements on an array model in order to be treated as periodic has been investigated by Holter and Steyskal [25].

In this thesis an active periodic structure – the endfire antenna – is investigated. The industry has identified a need for new software providing full wave simulations for very large group antennas, and the characterisation of the field from this simple endfire antenna is a step on the way towards developing more efficient algorithms. To put in context, we shall see later on that the software used in this thesis limits the number of elements in the antenna array to 256 using simple monopole elements. One may want to simulate group antennas with an order of 1000 elements with a more complex design.

1.2 The endfire antenna

An endfire antenna can be constructed of a large number of equal, equidistant antenna elements building up an array. The distance and phase difference between the elements are adapted to obtain constructive interference in one direction along the array and destructive interference in any other direction for the design frequency, in particular perpendicular to the array [10]. The antenna design is a result of the work by W.W. Hansen and J.R. Woodyard, published in their paper "*A new principle in directional antenna design*" [26]. In figure 1.1 the radiation pattern from such an endfire antenna, radiating in negative x direction, can be seen.

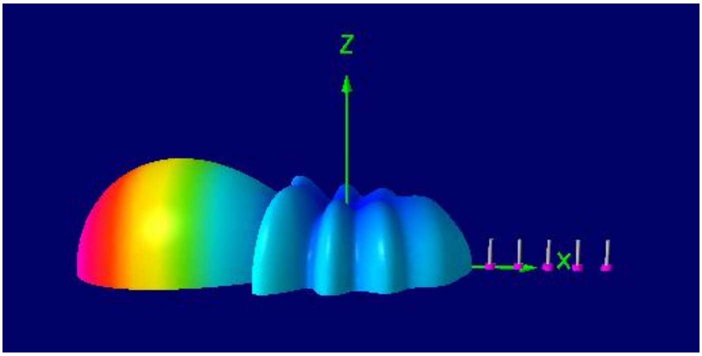

Figure 1.1 - Radiation pattern from an endfire antenna consisting of 10 monopoles over a perfectly conducting ground plane.

Endfire antennas are used for example in Airborne Early Warning and Control (AEW&C) systems, where it covers a gap of a total of 60 degrees at the nose and tail of the aircraft left by the side-looking antennas. The side-looking, so called broadside, antennas are also examples of periodic array antennas. The difference in distance and phase between the antenna elements are in this case adapted to direct the power outwards, orthogonal to the antenna extension [21, 22]. Figure 1.2 is a picture of two airplanes from the Royal Australian Air Force, equipped with a combination of broadside and endfire antennas.

Figure 1.2 - A Boeing 737 AEW&C plane with cavity endfire arrays (the surf board shaped "hat"). Image from http://en.wikipedia.org/wiki/File:Boeing_737_AEW%26C_Avalon.jpg. Published under the terms of the GNU Free Documentation License, Version 1.2.

1.3 Questions

The main question to be answered within the frames of this thesis is if a large, but finite, periodic structure can be analysed by a representative unit cell. If so, how can the fields in different unit cells be related to each other? Is there a significant difference to the case of a passive periodic structure? The edge elements are of special interest, since they are the difference between a finite and an infinite array. What effect does the presence of edge elements have? Is there a region on the antenna that can be characterized as periodic, with no or little influence from the edge elements? What phenomena can be observed on a finite end-fire antenna? Can some or all of them be observed in an infinite setting (analysis in a unit cell)?

1.4 Restrictions

The arrays investigated in this thesis are all of the simplest form, consisting of monopoles over a perfectly conducting ground plane. More complex structures are not considered. Limitations in the simulation software used, which will be described further on, set a maximum array length of 256 elements.

1.5 Report outline

This chapter has given a short introduction to the subject of this thesis. Chapter 2 presents some theory for electromagnetic waves before continuing with general antenna theory and narrowing down to dipoles and monopoles. At the end, periodic structures are briefly discussed along with some numerical methods. Chapter 3 describes the endfire antenna in more detail. In chapter 4, the geometrical properties and definitions of the antenna are given together with an overview of how the data was simulated and analysed. This chapter also states the hypotheses tested. Chapter 5 presents the results of the simulations accompanied with a discussion. Finally, chapter 6 summarises the conclusions drawn and provides an outlook for future work.

1.6 The authors' contribution

We have both participated in discussions concerning all parts of the work and in running simulations. Ahmed focused more on literature search and writing of the theory part of the report, and Ellinor on the method and results parts of the report along with writing scripts for generation of input files and analysis of the data.

2

2 Theory

2.1 Electromagnetic field theory

An EM field can be divided into the electric field $\boldsymbol{E}$ and the magnetic field $\boldsymbol{H}$. These fields are generated by interactions between the moving electrically charged particles and bound charges in materials [3]. Maxwell's equations in differential form [2],

$$\nabla \times \boldsymbol{E}(\boldsymbol{r},t) = -\frac{\partial \boldsymbol{B}(\boldsymbol{r},t)}{\partial t} \tag{2-1a}$$

$$\nabla \times \boldsymbol{H}(\boldsymbol{r},t) = \frac{\partial \boldsymbol{D}(\boldsymbol{r},t)}{\partial t} + \boldsymbol{J}(\boldsymbol{r},t) \tag{2-1b}$$

$$\nabla \cdot \boldsymbol{D}(\boldsymbol{r},t) = \rho(t) \tag{2-1c}$$

$$\nabla \cdot \boldsymbol{B}(\boldsymbol{r},t) = 0, \tag{2-1d}$$

govern the macroscopic propagation behaviour of EM waves in the point $\boldsymbol{r}$ at the time t. Here the vectors $\boldsymbol{E}, \boldsymbol{B}, \boldsymbol{H}, \boldsymbol{D}, \boldsymbol{J}$ and the scalar quantity $\rho(t)$ are defined as follows:

$\boldsymbol{E}(\boldsymbol{r},t) =$ Electric field [V/m]
$\boldsymbol{B}(\boldsymbol{r},t) =$ Magnetic flux density [Vs/m^2]
$\boldsymbol{H}(\boldsymbol{r},t) =$ Magnetic field [A/m]
$\boldsymbol{D}(\boldsymbol{r},t) =$ Electric flux density [As/m^2]

$\boldsymbol{J}(\boldsymbol{r},t) =$ Electric current density [A/m^2]
$\rho(t) =$ Electric charge density [As/m^3]

Equation (2-1a) is the differential form of Faraday's law of induction, which in its integral form states that a time-varying magnetic field through any surface S bounded by a closed path C gives rise to an electric field. The corresponding integral form of Faraday's law is

$$\oint_C \boldsymbol{E}(\boldsymbol{r},t) \cdot d\boldsymbol{l} = -\frac{d}{dt}\int_S \boldsymbol{B}(\boldsymbol{r},t) \cdot d\boldsymbol{S}. \tag{2-2a}$$

Equation (2-1b), called Ampere's law, states that a path integral of the magnetic field is equal to the sum of the current enclosed with that path plus the displacement current. Ampere's law on integral form is

$$\oint_C \boldsymbol{H}(\boldsymbol{r},t) \cdot d\boldsymbol{l} = \int_S \boldsymbol{J}(\boldsymbol{r},t) \cdot d\boldsymbol{S} + \frac{d}{dt}\int_S \boldsymbol{D}(\boldsymbol{r},t) \cdot d\boldsymbol{S}. \tag{2-2b}$$

Equation (2-1c) is Gauss law for electric field, which states that the surface integral of the electric flux around a closed surface S is equal to the charge generated by that surface, and (2-1d) state that the magnetic field $\boldsymbol{B}$ is divergence free [7],

$$\oint_S \boldsymbol{D}(\boldsymbol{r},t) \cdot d\boldsymbol{S} = \int_V \rho \, dv \tag{2-2c}$$

$$\oint_S \boldsymbol{B}(\boldsymbol{r},t) \cdot d\boldsymbol{S} = 0. \tag{2-2d}$$

Maxwell's equations, presented above, are valid in any kind of media. There are three physical phenomena that affect a medium in which EM waves propagate. These phenomena are electric polarization, magnetization, and electric conduction, and they are discussed in detail in [7].

In order to solve Maxwell's equations in free space or inside a material with a unique solution, the number of unknown vector parameters must be the same as the number of equations. For this purpose, constitutive equations are needed. [3]

For linear isotropic dielectrics and magnetic materials, the constitutive relation relates the electric and magnetic flux densities $\boldsymbol{D}$ and $\boldsymbol{B}$ with the electric and magnetic fields $\boldsymbol{E}$ and $\boldsymbol{H}$ as [6]

$$\boldsymbol{D} = \varepsilon_r \varepsilon_0 \boldsymbol{E} \qquad (2\text{-}3a)$$
$$\boldsymbol{B} = \mu_r \mu_0 \boldsymbol{H} \qquad (2\text{-}3b)$$

where ε_0 and μ_0 are the electric permittivity and magnetic permeability of free space, respectively, with the numerical values $\varepsilon_0 \approx 8.854 \cdot 10^{-12}$ F/m and $\mu_0 = 4\pi \cdot 10^{-7}$ H/m. The relative permittivity and permeability are denoted by ε_r and μ_r, respectively, and they are both equal to one in free space. These parameters represent the effect of polarization $\boldsymbol{P}$ and magnetization $\boldsymbol{M}$ inside a material and are related to the electric and magnetic susceptibilities, χ_e and χ_m, of the material according to

$$\varepsilon_r = 1 + \chi_e \qquad (2\text{-}4a)$$
$$\mu_r = 1 + \chi_m. \qquad (2\text{-}4b)$$

The velocity c of EM waves depends on the material where they propagate, according to $c = \frac{1}{\sqrt{\varepsilon_0 \mu_0 \varepsilon_r \mu_r}}$. $\boldsymbol{P}$ and $\boldsymbol{M}$ produces a secondary electric and magnetic field that acts in superposition with the applied field, and are related to $\boldsymbol{D}$ and $\boldsymbol{B}$ according to [3]

$$\boldsymbol{P} = \boldsymbol{D} - \varepsilon_0 \boldsymbol{E} \qquad (2\text{-}5a)$$
$$\boldsymbol{M} = \frac{\boldsymbol{B}}{\mu_0} - \boldsymbol{H}. \qquad (2\text{-}5b)$$

2.1.1 Boundary between two media

Maxwell's equations in differential form are valid at points in a continuous medium [7]. For a discontinuous medium, Maxwell's equations in integral form can be employed and used to derive the boundary conditions for the electromagnetic fields between two media with different dielectric parameters. The theory about boundary conditions is described in detail in [2] and [7], and the boundary conditions of the $\boldsymbol{E}$ and $\boldsymbol{H}$ fields between two media is shown in figure 2.1 and given as

$$\hat{\boldsymbol{n}} \times (\boldsymbol{E_1} - \boldsymbol{E_2}) = \boldsymbol{0} \qquad (2\text{-}6a)$$
$$\hat{\boldsymbol{n}} \times (\boldsymbol{H_1} - \boldsymbol{H_2}) = \boldsymbol{J_S} \qquad (2\text{-}6b)$$
$$\hat{\boldsymbol{n}} \cdot (\boldsymbol{D_1} - \boldsymbol{D_2}) = \rho_S \qquad (2\text{-}6c)$$

$$\hat{\boldsymbol{n}} \cdot (\boldsymbol{B_1} - \boldsymbol{B_2}) = \boldsymbol{0} \tag{2-6d}$$

where $\hat{\boldsymbol{n}}$ is the normal unit vector to the surface between two media directed from medium 2 into medium 1, $\boldsymbol{J_S}$ [As/m^2] is the surface current density and ρ_S [A/m] the surface charge density.

Equations (2-6a) and (2-6d) in the boundary condition state that the tangential component of the electric field $\boldsymbol{E}$ and the normal component of the magnetic flux density $\boldsymbol{B}$ between two media are continuous across the interface. The tangential component of the magnetic field $\boldsymbol{H}$ and the normal component of the flux density $\boldsymbol{D}$ are discontinuous by the amount of $\boldsymbol{J_S}$ and ρ_S respectively [6].

In a special case, when the second medium is a perfect electric conductor (PEC), all fields belonging to medium 2 vanishes ($\boldsymbol{E_2}$=$\boldsymbol{H_2}$=$\boldsymbol{D_2}$=$\boldsymbol{B_2}$=$\boldsymbol{0}$) and the boundary conditions take the form [3]

$$\hat{\boldsymbol{n}} \times \boldsymbol{E_1} = \boldsymbol{0} \tag{2-7a}$$
$$\hat{\boldsymbol{n}} \times \boldsymbol{H_1} = \boldsymbol{J_S} \tag{2-7b}$$
$$\hat{\boldsymbol{n}} \cdot \boldsymbol{D_1} = \rho_S \tag{2-7c}$$
$$\hat{\boldsymbol{n}} \cdot \boldsymbol{B_1} = \boldsymbol{0}. \tag{2-7d}$$

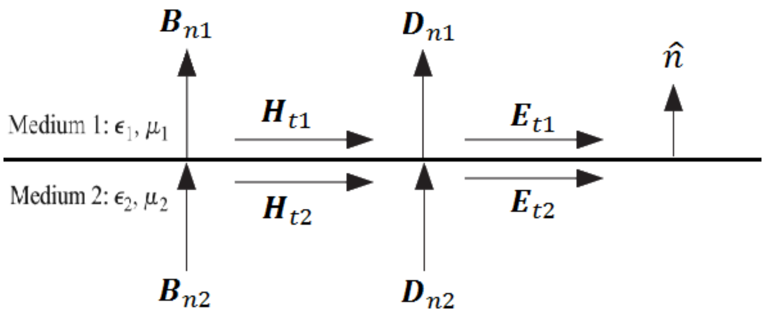

Figure 2.1 - Boundary condition at the interface between two media.

Maxwell's equations has two equations containing time-derivatives. In order to solve Maxwell's equations, the electric field will be assumed to be complex vectors with time-harmonic source dependenc $e^{j\omega t}$, as is done in [7]. The simplest way is to solve Maxwell's equations in the frequency domain instead of the time domain, by replacing the time derivative in the time domain with corresponding ωt in the frequency domain. The boundary conditions remain, since they do not contain any time derivatives and the electric field in the frequency domain is given by [7] as

$$\boldsymbol{E}(\boldsymbol{r},t) = Re(\boldsymbol{E}(\boldsymbol{r},\omega)e^{j\omega t}) \tag{2-8}$$

Maxwell's equations in frequency-domain with electric field assumption become

$$\nabla \times \boldsymbol{E}(\boldsymbol{r},\omega) = -j\omega\boldsymbol{B}(\boldsymbol{r},\omega) \tag{2-9a}$$
$$\nabla \times \boldsymbol{H}(\boldsymbol{r},\omega) = j\omega\boldsymbol{D}(\boldsymbol{r},\omega) + \boldsymbol{J}(\boldsymbol{r},\omega) \tag{2-9b}$$
$$\nabla \cdot \boldsymbol{D}(\boldsymbol{r},\omega) = \rho(\omega) \tag{2-9c}$$
$$\nabla \cdot \boldsymbol{B}(\boldsymbol{r},\omega) = 0 \tag{2-9d}$$

2.2 Antenna theory

2.2.1 Field regions

There are three regions surrounding the antenna: reactive near-field, radiating near field (Fresnel) and far-field (Fraunhofer) [8]. Figure 2.2 is inspired by [8] and shows the different antenna regions. There are no actual discontinuities between these three regions, and the boundary between them is not very rigid. The derivation of the boundary between these regions is shown in detail in [17].

The immediate field surrounding the antenna is called reactive near field, wherein the reactive field term predominates. The outer boundary of this region is at a distance

$$R < 0.62\sqrt{\frac{D^3}{\lambda}} \tag{2-10}$$

from the origin where D is the largest dimension of the antenna. For a very short dipole, the outer boundary is at a distance $R < \frac{\lambda}{2\pi}$ [8].

The middle region between the reactive near field and the far field is the radiating near field or Fresnel Region, and the radius of this region satisfy the condition

$$0.62\sqrt{\frac{D^3}{\lambda}} < R < \frac{2D^2}{\lambda} \quad (2\text{-}11)$$

This region may not exist in the case of small antenna dimension compared to the wavelength [8].

Far away from the antenna, with $R \geqslant \frac{2D^2}{\lambda}$, is the far field or Fraunhofer region. In this region the radiation pattern does not change with the distance from the antenna, and the wave travelling from the antenna takes a plane form.

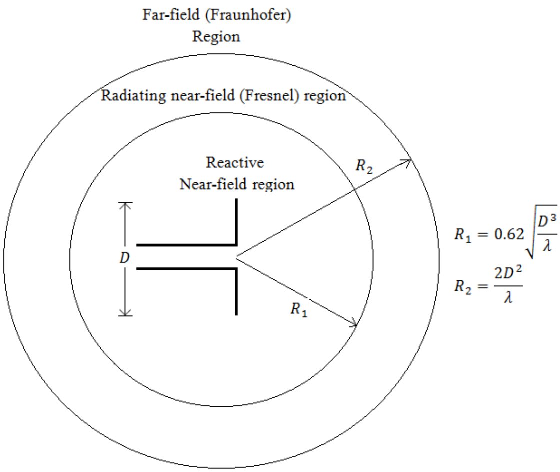

Figure 2.2 - Antenna regions: reactive near field, radiating near field and far field. Inspired by [8].

2.2.2 Radiation from general source distribution

The theory of this section is extracted from [6] where the radiation from a general current source is studied in detail. The radiated electromagnetic fields $\boldsymbol{E}$ and $\boldsymbol{H}$ for a given source distribution of currents and charges can be obtained directly by solving Maxwell's equations in differential form for given constitutive relations and boundary conditions. However, it is often more convenient and easier to solve equations 2-1c and 2-1d by determination of the electric and magnetic potential

$\boldsymbol{\phi(r)}$ and $\boldsymbol{A(r)}$ first, rather than the $\boldsymbol{E}$ and $\boldsymbol{H}$ fields. Figure 2.3 is based on [6] and illustrates the generated electric and magnetic potentials from a given current or charge distribution. The potentials $\boldsymbol{\phi(r)}$ and $\boldsymbol{A(r)}$ are given in [7] with a sinusoidal time dependence $e^{j\omega t}$ for these two quantities,

$$\phi(\boldsymbol{r}) = \int_V \frac{\rho(\boldsymbol{r}')e^{-jk|\boldsymbol{r}-\boldsymbol{r}'|}}{4\pi\varepsilon_0|\boldsymbol{r}-\boldsymbol{r}'|} dV' \qquad (2\text{-}12a)$$

$$\boldsymbol{A}(\boldsymbol{r}) = \int_V \frac{\mu_0 \boldsymbol{J}(\boldsymbol{r}')e^{-jk|\boldsymbol{r}-\boldsymbol{r}'|}}{4\pi|\boldsymbol{r}-\boldsymbol{r}'|} dV' \qquad (2\text{-}12b)$$

where k is the free-space wave number, related to the wavelength λ via $k = \frac{2\pi}{\lambda}$, $\boldsymbol{r}$ is the location of the field point and $\boldsymbol{r'}$ is a vector from the origin to the source point. Only the magnetic potential $\boldsymbol{A(r)}$ is needed in order to determine the $\boldsymbol{E}$ and $\boldsymbol{H}$ fields.

The far field approximation of the magnetic potential for the antenna can be determined by assuming $\boldsymbol{r} \gg \boldsymbol{r}'$,

$$\boldsymbol{A}(\boldsymbol{r}) = \frac{\mu_0 e^{-jkr}}{4\pi r} \int_V \boldsymbol{J}(\boldsymbol{r}')e^{jk\boldsymbol{r}'\cdot\hat{\boldsymbol{r}}}\, dV'. \qquad (2\text{-}13)$$

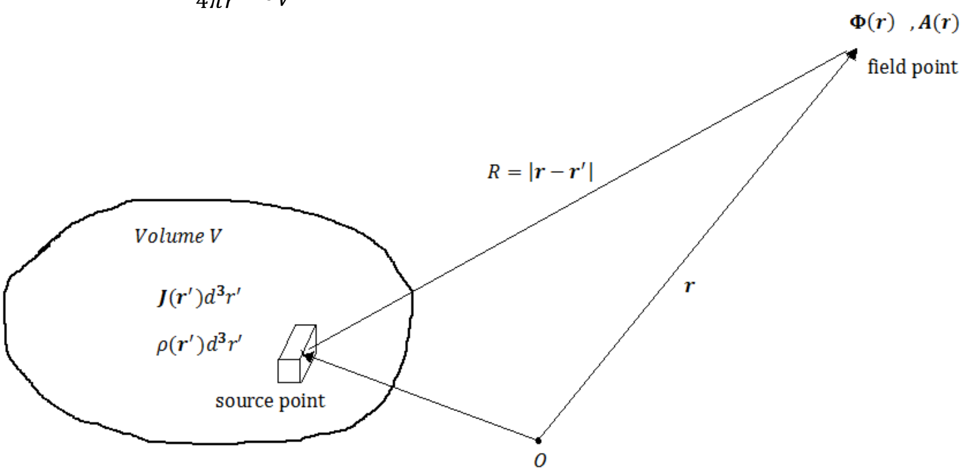

Figure 2.3 - Electric and magnetic potential, $\phi(r)$ and $A(r)$, generated by current and charge distribution.

$\boldsymbol{A}(\boldsymbol{r})$ is a 3-dimensional spatial Fourier transform for the current densities of the antenna [3]. The volume integral term of equation 2-13 is called radiation vector, denoted by $\boldsymbol{F}(\theta, \phi)$, and is dependent on the polar and azimuth angles. Then the $\boldsymbol{E}$ and $\boldsymbol{H}$ fields can be obtained from the magnetic potential by

$$\boldsymbol{E} = -jk\eta(\hat{\boldsymbol{r}} \times \boldsymbol{A}) \times \hat{\boldsymbol{r}} \tag{2-14a}$$
$$\boldsymbol{H} = -jk\, \hat{\boldsymbol{r}} \times \boldsymbol{A}, \tag{2-14b}$$

where $\hat{\boldsymbol{r}}$ is the wave propagation direction with impedance $\eta = \sqrt{\frac{\mu}{\epsilon}} = \frac{|\boldsymbol{E}|}{|\boldsymbol{H}|}$. The relation between the $\boldsymbol{E}$ and $\boldsymbol{H}$ fields for a plane wave is

$$\boldsymbol{E} = \eta \boldsymbol{H} \times \hat{\boldsymbol{r}} \tag{2-15}$$

Thus, the $\boldsymbol{E}$ and $\boldsymbol{H}$ fields in the far region are given as

$$\boldsymbol{E} = -jk\eta\left(A_\theta \hat{\boldsymbol{\theta}} + A_\phi \hat{\boldsymbol{\phi}}\right) \tag{2-16a}$$
$$\boldsymbol{H} = -\frac{j\omega}{\eta} \hat{\boldsymbol{r}} \times \left(A_\theta \hat{\boldsymbol{\theta}} + A_\phi \hat{\boldsymbol{\phi}}\right) \tag{2-16b}$$

2.2.3 Terminology

An antenna can be described in terms of radiation characteristics for receiving and transmitting electromagnetic waves, or in terms of a circuit element where the antenna is connected to the transmission line. In order to determine the electric far-field from an antenna structure, the radiation vector $\boldsymbol{F}(\theta, \phi)$ for a current distribution is given by [6] as a volume integral of the current distribution around the antenna,

$$\boldsymbol{F}(\theta, \phi) = \boldsymbol{F}(\hat{\boldsymbol{r}}) = \int_V \boldsymbol{J}(\boldsymbol{r}')\, e^{jk\hat{\boldsymbol{r}}\cdot\boldsymbol{r}'} dV'. \tag{2-17}$$

The electric far field from the antenna is then given by [6],

$$\boldsymbol{E}(\boldsymbol{r}) = -jk\eta_0 \frac{e^{-jkr}}{4\pi r} \boldsymbol{F}_\perp(\hat{\boldsymbol{r}}) = -jk\eta_0 \frac{e^{-jkr}}{4\pi r} (\hat{\theta} \boldsymbol{F}_\theta + \hat{\phi} \boldsymbol{F}_\phi), \tag{2-18}$$

where $\boldsymbol{F}_{\perp}$ denotes the component of $\boldsymbol{F}$ that is perpendicular to the propagation direction $\hat{\boldsymbol{r}}$. The radiation intensity $U(\theta,\phi\ )$ is defined as the angular distribution of the radiated power density around the antenna per unit solid and is given by [4]

$$U(\theta,\phi\ ) = \frac{\eta_0 k^2}{32\pi^2}|\boldsymbol{F}_{\perp}(\theta,\phi)|^2 \qquad \text{(2-19)}$$

The total radiated power $P_{rad}(\theta,\phi)$ can be determined by integration of the radiation intensity over a unit sphere,

$$P_{rad}(\theta,\phi) = \int_0^{\pi}\int_0^{2\pi} U(\theta,\phi)\sin\theta\, d\phi d\theta. \qquad \text{(2-20)}$$

It is interesting to describe the radiation of an antenna in a specific direction. The directivity $D(\theta,\phi)$ of an antenna is defined as the ratio between the radiation intensity in a specific direction, normalized by the average intensity, given by [4] as

$$D(\theta,\phi) = \frac{U(\theta,\phi\ )}{P_{rad}(\theta,\phi)/4\pi}. \qquad \text{(2-21)}$$

The radiation pattern is omni-directional when the directivity is independent of the angles θ and ϕ. This cannot occur for real antennas, where typically at most a pattern independent of azimuthal angle ϕ can be achieved.

The gain $G(\theta,\phi)$ of an antenna is defined as the radiation intensity normalized by the power accepted by the antenna, P_T,

$$G(\theta,\phi) = \frac{U(\theta,\phi\ )}{P_T/4\pi}. \qquad \text{(2-22)}$$

The relation between the gain and the directivity is

$$G(\theta,\phi) = \eta D(\theta,\phi) \qquad \text{(2-23)}$$

where η is the antenna efficiency that describes the losses of the antenna, and it is defined as a ratio between the radiation power and the input power. For a lossless dipole ($\eta = 1$) the gain and the directivity are the same.

An antenna can also be described as a circuit element where the antenna is connected to a transmission line. The input impedance Z of an antenna relates the relation between voltage and current at the input to the antenna. It varies with frequency and is often a complex number,

$$Z = R + jX \tag{2-24}$$

where the real part is the resistance R, related to the dissipation of power due to the radiation or absorption of electromagnetic waves and the material losses, and the imaginary X part relates the power stored in the near field around the antenna [1]. The reflection of the power back to the transmission line depends on the difference between the antenna input impedance and the characteristic impedance Z_0 of the transmission line, where the maximum power transfer is achieved when the difference is zero [1].

2.2.4 Image theory

A current distribution above an infinite perfect conducting ground plane creates an image of identical current distribution. The image theory is based on the boundary condition on the surface of the perfect electric conductor (PEC) or perfect magnetic conductor (PMC). The boundary conditions that are the tangential component of the electric field is zero on the surface of a PEC, and the tangential component of the magnetic field is zero on the surface of a PMC. This way, the ground plane can be replaced by an image current placed below the ground plane at equal distance. For a PEC, the direction of the image electric current distribution of the electric current perpendicular to the ground plane is the same, whereas the direction of the image electric current distribution of horizontal electric current is opposite [2, 7]. In figure 2.4, based on [3], the electric and magnetic current densities are presented.

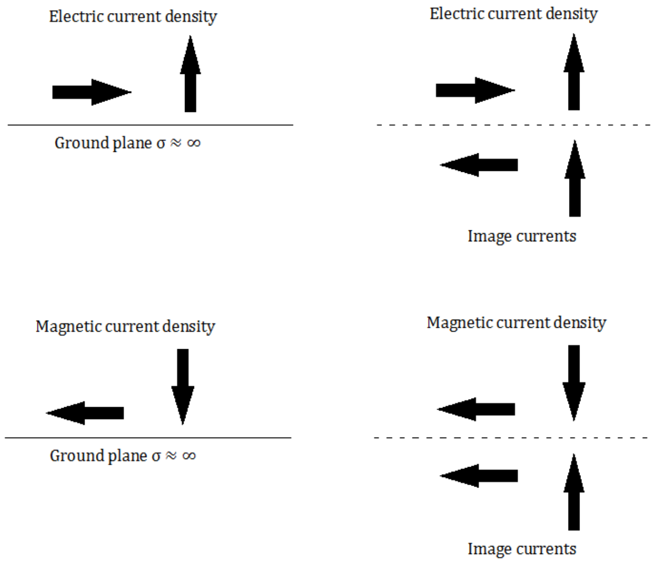

Figure 2.4 - Electric and magnetic current densities above an infinite ground plane.

2.2.5 Radiation from a wire dipole antenna

The wire dipole antenna is a simple and classic form of antenna. It consists of a thin linear wire with a center feed or an end feed point. Some examples of wire antennas are hertzian dipole, folded dipole and monopole antennas. The most studied type is the half wave dipole, since it is a self-resonance of a thin dipole [6].

For an infinitely thin wire antenna with center feed point and length l, directed on the z axis, the current density can be approximated by

$$\boldsymbol{J}(\boldsymbol{r}) = \hat{\mathbf{z}} I(z)\delta(x)\delta(y) \tag{2-25}$$

where $I(z)$ is the current distribution along the wire antenna. The radiation vector will have only a z component, since the wire is directed on the z axis, and the radiation vector is given by

$$F_z(\theta) = \int_{-l/2}^{l/2} I(z') e^{jk_z z'} dz' = \int_{-l/2}^{l/2} I(z') e^{jkz' \cos\theta} dz' \tag{2-26}$$

by using spherical coordinates to resolve $\hat{\mathbf{z}}$ and identify the component of the radiation vector in spherical coordinates. The obtained radiation vector depends on the polar angle θ and is independent of the azimuthal angle ϕ (omni-directional). The radiated electric and magnetic field generated by a wire antenna is shown in figure 2.5, and is given by

$$\boldsymbol{E} = \widehat{\boldsymbol{\theta}}E_{\boldsymbol{\theta}} = \widehat{\boldsymbol{\theta}}jk\eta\frac{e^{-jkr}}{4\pi r}F_z(\theta)\sin\theta \tag{2-27a}$$

$$\boldsymbol{H} = \widehat{\boldsymbol{\phi}}H_{\phi} = \widehat{\boldsymbol{\phi}}jk\frac{e^{-jkr}}{4\pi r}F_z(\theta)\sin\theta. \tag{2-27b}$$

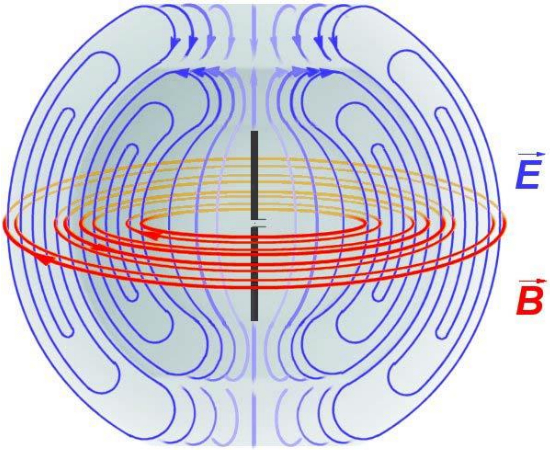

Figure 2.5 - Electric and magnetic field radiated from a dipole antenna. (Image from http://de.wikipedia.org/wiki/Datei:Felder_um_Dipol.jpg by user Averse. Published under the terms of the GNU Free Documentation License, Version 1.2.)

2.2.6 Half-wave dipole antenna

The half wave dipole antenna is the most common type of wire antenna. In order to determine the radiation intensity, directivity and the radiated field of a half wave dipole, the current distribution around the antenna should be approximated so that the current at the ends of the dipole vanishes and the maximum current is on the middle of the dipole. For a z-directed antenna with length l and feed point on the origin, a good approximation is a sinusoidal current distribution along the antenna according to [5],

$$\mathrm{I(z) = I_0 \sin k\,(l - |z|),\ l/2 \geq\ z \geq -l/2.} \tag{2-28}$$

This approximation is valid as long as the dipole is not too long and the radius is thin. The z component of the radiation vector for a half wave dipole is simplified to

$$F_z(\theta) = \frac{2I_0}{k}\frac{\cos\left(\frac{\pi}{2}\cos\theta\right)}{sin^2\theta} \tag{2-29}$$

after using $kl = \pi$ where $l = \lambda/2$. The radiation pattern of a half wave dipole is omni-directional, and the maximum directivity occurs when the azimuthal angle is $\frac{\pi}{2}$ (in the horizontal plane),

$$D = D\left(\frac{\pi}{2}, \phi\right) \approx 1.64 = 2.15\ dB \tag{2-30}$$

as shown in figure 2.6.

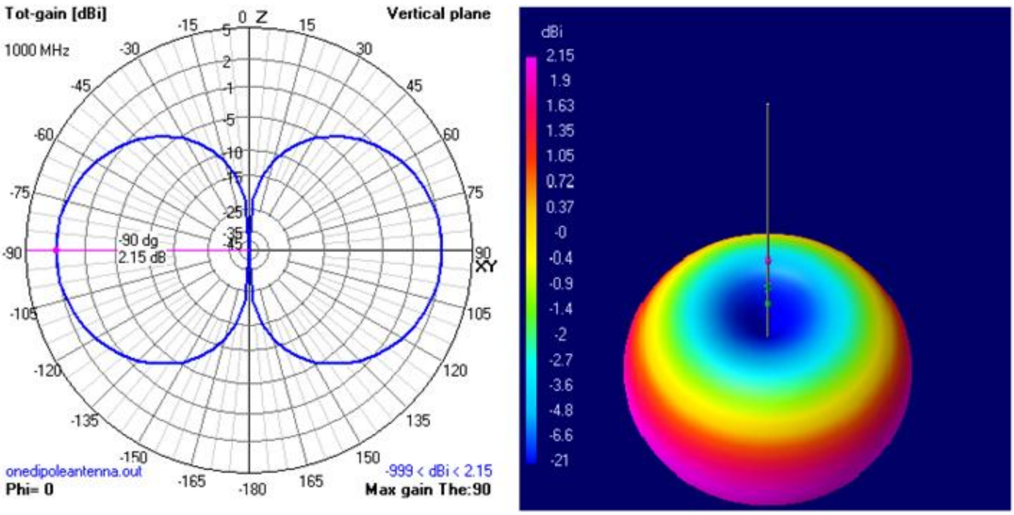

Figure 2.6 - Radiation pattern from a half-wave dipole. In the left picture, depicting the total gain for different θ, the dipole is in the z-direction and the xy plane orthogonal to this page.

2.2.7 Monopole antenna

A monopole antenna is one half of a dipole antenna and consists of a single conductor fed out of a ground plane. The feed for a monopole antenna can be a coaxial line with an inner conductor connected to the monopole, and the outer conductor connected to the ground plane. By using image theory a monopole antenna over an infinite perfect ground plane can be replaced by a dipole with a center feed point. The current distribution in a monopole antenna can also be approximated with a sinusoidal current distribution when the monopole is very thin ($r < l/30$) and not too long ($l < \lambda/4$) [5].

The input impedance of a monopole decreases to one-half compared with a half-wave dipole, since only half of the voltage is required to drive a monopole compared with a dipole, and the same current is produced. The gain and directivity of a monopole antenna is twice as much as the corresponding dipole antenna, since the electric field vanishes below the ground plane and needs a half of the input power to produce the same electric field [4]. Figure 2.7 shows the radiation pattern from a monopole over ground plane.

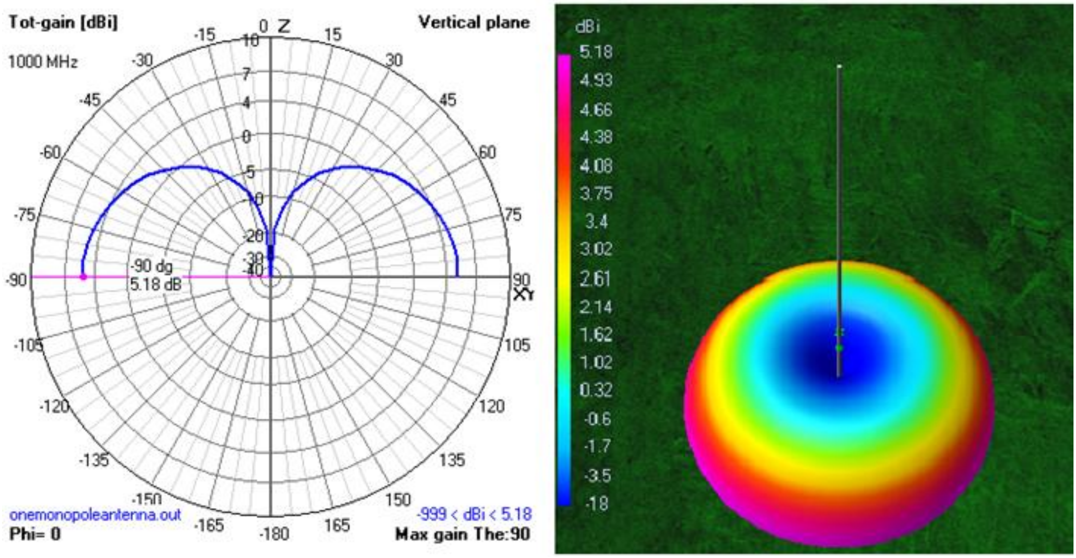

Figure 2.7 - Radiation pattern from a quarter-wave monopole over a perfectly conducting ground plane. In the left picture, depicting the total gain for different θ, the monopole is in the z-direction and the xy plane orthogonal to this page and coinciding with the ground plane.

2.3 Method of Moments

Only a few problems regarding radiation of EM waves can be solved analytically. There are several powerful numerical methods for determining the radiation of EM fields around an antenna structure. The Finite Element Method (FEM) and the Method of Moments (MoM) are two of these.

For the simulations in this thesis, MoM is used. The theory is described in detail in [7], [12] and [8]. The idea for solving integral equations is to convert these equations into a linear system that can be solved numerically using a computer program.

In section 2.2.1 it is described how the electric and magnetic potential $\phi(\boldsymbol{r})$ and $\boldsymbol{A}(\boldsymbol{r})$ are calculated from known $\boldsymbol{J}$ and ρ. To determine these $\boldsymbol{J}$ and ρ, MoM is used. The radiation and scattering problems around an antenna should be expressed as integral equations, the electric and magnetic field integral equations, EFIE and MFIE, respectively. EFIE and MFIE for a perfect electric conducting body is given in [8] as

$$\widehat{\boldsymbol{n}} \times \boldsymbol{E}^{inc}|_{\text{surface}} = -\widehat{\boldsymbol{n}} \times \frac{\nabla(\nabla\cdot\boldsymbol{A})+k^2\boldsymbol{A}}{j\omega\varepsilon}|_{\text{surface}} \tag{2-31a}$$

$$\widehat{\boldsymbol{n}} \times \boldsymbol{H}^{inc}|_{\text{surface}} = \boldsymbol{J} - \widehat{\boldsymbol{n}} \times (\nabla \times \boldsymbol{A})|_{\text{surface}} \tag{2-31b}$$

where $\boldsymbol{E}^{inc}$ and $\boldsymbol{H}^{inc}$ are the incident fields for the receiving antenna or field from the feed, ε and μ are electric permittivity and magnetic permeability of the medium respectively, k is the wave number of the medium given by $k = \omega\sqrt{\varepsilon\mu}$, $\boldsymbol{J}$ is the induced surface current density (unknown parameter), $\widehat{\boldsymbol{n}}$ is the outward normal unit vector, and $\boldsymbol{A}$ is a magnetic vector potential function at distance R from a point (s', t') on the surface to the point (x, y, z) where the field is evaluated and given by

$$\boldsymbol{A}(x, y, z) = \iint_{\text{surface}} \boldsymbol{J}(s', t') \frac{e^{-jkR}}{4\pi R} ds'dt' \tag{2-32}$$

where s and t are parametric variables on the surface. The vector integral equations for EFIE and MFIE have a linear system form,

$$L\{\boldsymbol{J}\} = \boldsymbol{V}, \tag{2-33}$$

where L is a linear vector operator and $\boldsymbol{V}$ is the excitation function, where $\boldsymbol{E}^{inc}$ is included in $\boldsymbol{V}$ for a scattering problem. In order to solve a linear equation system, the equations should be converted into a matrix form. By a discretisation of the current distribution $\boldsymbol{J}$ by a series of a linearly independent vector basis functions $\boldsymbol{B}_n(s, t)$ along the surface of the antenna as

$$\boldsymbol{J}(s, t) \cong \sum_{n=1}^{N} I_n \boldsymbol{B}_n(s, t) \tag{2-34}$$

where I_n is the unknown parameter. These parameters can be determined by scalar multiplication with a vector testing function, $\boldsymbol{T}_m(s,t)$, and integration over the surface of the antenna,

$$\iint_{\text{surface}} \boldsymbol{T}_m \cdot L\{\boldsymbol{J}\}\, dsdt = \iint_{\text{surface}} \boldsymbol{T}_m \cdot \boldsymbol{V}\, dsdt, \qquad m = 1,2,3,\ldots\ldots,N \tag{2-35}$$

This can be rewritten in a matrix form as

$$\begin{bmatrix} Z_{11} & Z_{12} & \cdots & \cdots & \cdots & Z_{1N} \\ Z_{21} & Z_{22} & \cdots & \cdots & \cdots & Z_{2N} \\ \cdot & \cdot & \cdots & \cdots & \cdots & \cdots \\ \cdots & \cdots & \cdots & \cdots & \cdots & \cdots \\ Z_{N1} & \cdots & \cdots & \cdots & \cdots & Z_{NN} \end{bmatrix} \begin{bmatrix} I_{1N} \\ I_{2N} \\ \vdots \\ I_{N1} \end{bmatrix} = \begin{bmatrix} V_{1N} \\ V_{2N} \\ \vdots \\ V_{N1} \end{bmatrix} \tag{2-36}$$

$$Z_{mn} = \iint_{\text{surface}} \boldsymbol{T}_m \cdot L\,\{\boldsymbol{B}_n\} dsdt$$

$$V_m = \iint_{\text{surface}} \boldsymbol{T}_m \cdot \mathbf{V}\, dsdt$$

The current density $\boldsymbol{J}(s,t)$ on the surface of the antenna can be solved numerically by MoM.

The main advantage of using MoM compared with other methods, like FEM, for solving a radiation problem lies in the meshing. In FEM, the whole body, including the air between and above the monopoles, must be divided into 3D segments, modelled, and solved for in order to calculate the field. Doing so for large structures requires a great deal of computer capacity, and as all segments need a boundary the surrounding free space must be truncated and a virtual boundary must be introduced [8]. Using MoM, only the surface of the antenna structure needs to be meshed.

2.4 Periodic structures

Periodic structures have been used in many applications in science and engineering to simplify many physical concepts. They classify into passive and active periodic structures. Periodic structures find application in a variety of devices such as microwave filter networks [2], crystal structures [24], and reflection and transmission in dielectric mirrors, studied in detail in [6], and are some examples of passive periodic structures [14]. An antenna array is an example of an active periodic structure.

Propagation of EM waves in active and passive periodic structures are based on Floquet's theorem and studied in [15]. The circuit representation for 1D passive periodic structures in z direction have equal elements spaced periodically with period d. By letting $E(z)$ be the field reacting with the periodic surface, the field at each period can be represented by the field of the previous period multiplied by a constant, or more generally

$$E(z+nd) = C^n E(z) \tag{2-37}$$

where C is a constant, n is the period number for boundedness $|C| \leqslant 1$. In general $C = e^{jdK}$ where d is the period distance and K is a (possibly complex) constant called the Bloch wave number.

2.4.1 Microwave filter

A microwave filter is a passive periodic structure and is designed by two methods, the image parameter method and the insertion loss method. These methods are described in detail in [2]. Microwave filters consist of a transmission line or waveguide loaded with a cascade connection of identical two port networks with a finite number of reactive elements. However, it can be designed as a model with an infinite number of reactive elements as shown in figure 2.8.

For a wave propagating in the positive z direction, where the periodic structure is infinitely long the relation between the voltage and current in subsequent terminals is given by

$$V_{n+1} = V_n e^{-\gamma d} \tag{2-38}$$

$$I_{n+1} = I_n e^{-\gamma d} \tag{2-39}$$

where $\gamma = \alpha + j\beta$ is the complex propagation factor of the periodic structure, and d is the physical length of each individual section. This can be written in matrix form as

$$\begin{bmatrix} V_n \\ I_n \end{bmatrix} = \begin{bmatrix} A & B \\ C & D \end{bmatrix} \begin{bmatrix} V_{n+1} \\ I_{n+1} \end{bmatrix} = \begin{bmatrix} V_{n+1}e^{\gamma d} \\ I_{n+1}e^{\gamma d} \end{bmatrix} \tag{2-40}$$

where the matrix elements are given in [2],

$$A = \cos\theta - \frac{\mathrm{b}}{2}\sin\theta \tag{2-41a}$$

$$B = j\left(\frac{\mathrm{b}}{2}\cos\theta + \sin\theta - \frac{\mathrm{b}}{2}\right) \tag{2-41b}$$

$$C = j\left(\frac{\mathrm{b}}{2}\cos\theta + \sin\theta + \frac{\mathrm{b}}{2}\right) \tag{2-41c}$$

$$D = \cos\theta - \frac{\mathrm{b}}{2}\sin\theta \tag{2-41d}$$

where b is the susceptance, which is normalised to the characteristic impedance Z_0, $\theta = kd$ is the electrical length of the transmission line in the unit cell and k is the propagation constant of the unloaded line.

Depending on the complex propagation factor γ, if it is real ($\alpha \neq 0, \beta = 0$) or imaginary ($\alpha = 0, \beta \neq 0$), the propagating waves on the loaded line periodic structure exhibit either stopband or passband [2].

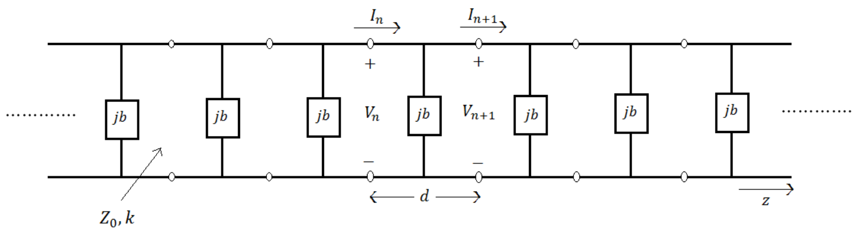

Figure 2.8 - A microwave filter, an infinite passive periodic structure.

2.4.2 Periodic Greens function

Electromagnetic scattering from periodic structures can be determined using an integral equation technique as the method described in section 2.3. The periodic Green's function (PGF) is an efficient and accurate computation method that is used in order to calculate the scattering of EM waves by a periodic structures, such as antenna arrays or photonic band-gap structures [11]. The application of the Floquet-Bloch theorem, studied in detail in [14], reduces the computational domain of an infinite periodic structure to a single unit cell, but requires the numerical evaluation of very slowly converging series [18].

The PGF for 3-D problem with 1-D periodic point sources along x direction with spatial period d and a constant phase shift β in free space is given in [18] as

$$G_p(\boldsymbol{r}) = \frac{1}{4\pi}\sum_{n=-\infty}^{+\infty}\frac{e^{-jk|\boldsymbol{r}-ndx_0|}}{|\boldsymbol{r}-ndx_0|}e^{-jn\beta d} \qquad (2\text{-}42)$$

where x_0 is the measuring point. The series diverge when the phase shift is complex. Three methods are discussed in [18] in order to accelerate the convergence of such series; these methods are Kummer-Poisson's decomposition, Ewald's method and an integral representation. All of these methods exhibit exponential convergences are valid in the general case of a complex phase shift between sources [18].

3

3 Endfire antennas

3.1 Antenna arrays

Array antennas are composed of two or more antenna elements, and are used to direct the radiated power in a desired direction. The radiated power is either broadside, where the maximum radiation is perpendicular to array orientation, or end-fire, where the maximum radiation is in the same direction as the array orientation. Most antenna arrays consist of identical antenna elements; a sketch of a one dimensional uniform linear monopole array with distance d between the elements and feed point in the end of each monopole is shown in figure 3.1.

There are several array design parameters which can be used to shape the overall array pattern, such as element geometrical arrangement, element spacing, and element relative excitation amplitude and phase. With these controlled parameters it is possible to obtain a required radiation pattern.

Assuming no coupling between the elements and that the current in each element is the same in an array, the total radiated field can be determined by the vector addition of the fields radiated by a single element in an array [10]. The theory of the radiated electric field from two and N element linear arrays is described in detail in [10]. Assuming coupling between elements of uniform amplitude and spacing, the total radiated field can be determined by using the array pattern multiplication property of identical elements. This means that the overall radiated field of an array can be obtained by multiplying the field of a single element with the array factor. The array factor is a function that depends on the controlled parameters above, and is not dependent on the type of antennas that constitute the array. The normalised array factor (AF) for a linear N element array with uniform amplitude and spacing distance d, where each succeeding element has progressive phase β, is given by [10]

$$(AF)_n = \frac{1}{N}\left[\frac{\sin\left(\frac{N}{2}\psi\right)}{\sin\left(\frac{1}{2}\psi\right)}\right] \tag{3-1}$$

where ψ is the array phase shift,

$$\psi = kdcos(\theta) + \beta, \tag{3-2}$$

and θ is the elevation angle.

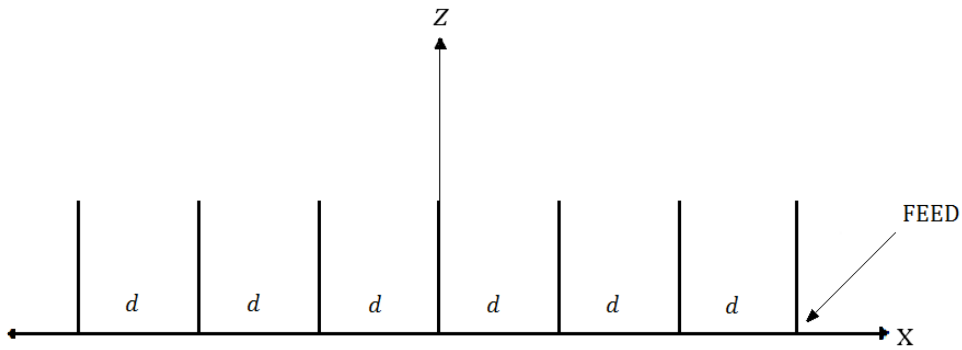

Figure 3.1 - A uniform linear monopole array antenna. Feed in $x = 0$ for all monopoles, as indicated for the leftmost.

Performance and behaviour of two kinds of antenna arrays, the ordinary end-fire (OEF) array and the Hansen-Woodyard end-fire (HWEF) array, will be discussed.

3.2 Ordinary endfire (OEF) array

Depending on the direction of maximum directivity, the phase shift between the elements in an array is adapted to cause constructive interference in the desired direction and destructive interference in the other directions.

The direction of the radiated power in an OEF array is along the axis, where $\theta = 0^o$ or $\theta = 180^o$. The progressive phase shift β of a uniform array can be determined by putting the array phase shift ψ to zero. The progressive phase shift depends on which direction the maximum radiation power will occur, according to

$$\beta = -kd \text{ for } \theta = 0^o \qquad (3\text{-}3)$$
$$\beta = kd \text{ for } \theta = 180^o.$$

The normalized array factor for an OEF array with N elements and the maximum radiation in $\theta = 0^o$ (negative sign) or $\theta = 180^o$ (positive sign) reduces to

$$(AF)_n \approx \frac{\sin\left[\frac{Nkd}{2}(\cos(\theta) \pm 1)\right]}{\left[\frac{Nkd}{2}(\cos(\theta) \pm 1)\right]}. \qquad (3\text{-}4)$$

The number of end-fire maxima depends on the spacing between elements in an array. The maximum distance between elements in an array is $d_{max} < \frac{\lambda}{2}$, if the desired number of end-fire maximum is one and without any grating lobes. The maximum radiation occurs in both directions (two end-fire maximum at $\theta = 0^o$ and $\theta = 180^o$) when the space between elements is $d = \frac{\lambda}{2}$. Maximum radiation occurs in both end-fire and broadside directions if the element spacing in an array is a multiple of a wavelength, $d = n\lambda$ where n is an integer.

The directivity of an OEF array is given in [8] as $D = 4\left(\frac{L}{\lambda}\right)$ where L is the length of the array assuming $L \gg d$. To achieve a better directivity of an OEF array, Hansen and Woodyard proposed a slightly modified phase shift and distance between the elements of an OEF array [10].

3.3 Hansen-Woodyard endfire (HWEF) array

In many applications, a higher directivity is required. To obtain this requirement, the progressive phase shift between array elements should be changed depending on the direction of the maximized directivity according to [10],

$$\beta = -\left(kd + \frac{2.94}{N}\right) \text{ for maximum at } \theta = 0°$$
$$\beta = +\left(kd + \frac{2.94}{N}\right) \text{ for maximum at } \theta = 180°. \quad (3\text{-}5)$$

These conditions are known as the Hansen-Woodyard conditions for end-fire radiation. These conditions lead to larger directivity than for the OEF array and ensure maximum directivity (minimum beamwidth) in the desired direction [10].

Another condition has to be complemented the H-W conditions to avoid the trade-off in the side lobe level, which is higher than the OEF array. The spacing between elements in the array should be approximately [10]

$$d = \left(\frac{N-1}{N}\right)\frac{\lambda}{4} \quad (3\text{-}6)$$

The directivity of a HWEF array is $D = 1.805\left[4\left(\frac{L}{\lambda}\right)\right]$. This means, by using HW-conditions, the directivity will be maximized by factor of 1.805 (or 2.5 dB) compared to an OEF array. A comparison governing the directivity between HWEF array and OEF array is shown in figure 3.2, using a uniform linear monopole array consisting of 99 elements. The bandwidth of the HWEF array becomes narrower compared to the OEF array according to [8].

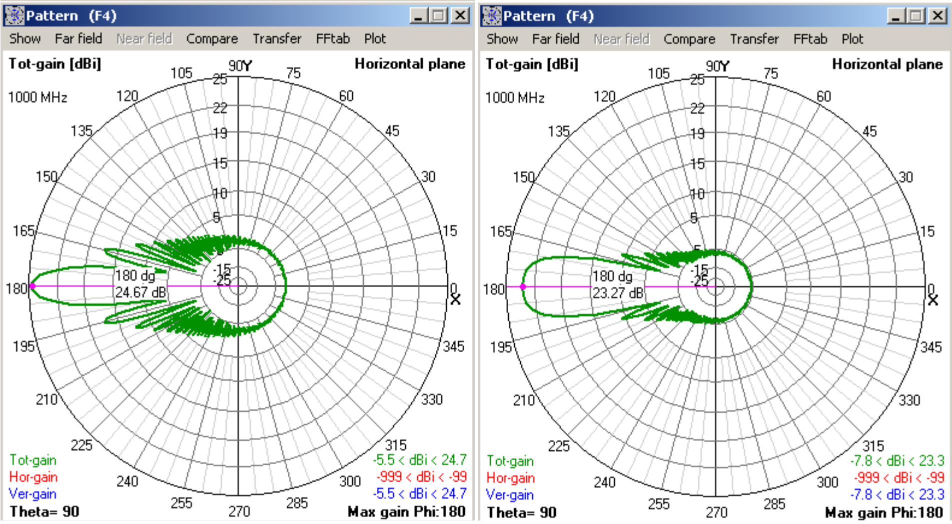

Figure 3.2 - Comparison between HWEF (left) and OEF (right) for an $N = 99$ antenna array seen from above, the array starting in $x = 0$ extending in positive and radiating in negative x direction.

4

4 Method

This chapter starts by defining all properties of the antenna structure needed for analysis, along with a description of the test data. After that follows a description of the software used for simulations, The Numerical Electromagnetics Code (NEC). Analysis of the data extracted from NEC was performed using MATLAB, based on the hypotheses presented in section 4.3, and an analysis outline is presented in the last section.

4.1 Statement of the problem

4.1.1 Geometry

Figure 4.1 illustrates and defines the geometrical properties of the studied endfire antenna, which follows the Hansen-Woodyard design. The array consists of N monopoles numbered $1..N$ along the x axis with a distance d between them, placed over a perfectly conducting ground in the xy-plane. Each monopole has a length l and the phase shift between two consecutive monopoles is denoted by β. Furthermore, the measuring points (marked by crosses) are at a height z_0 over the ground plane.

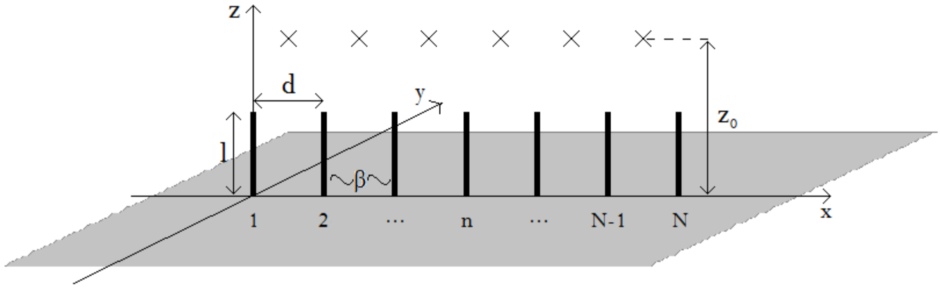

Figure 4.1 - Geometry of the endfire antenna. A Cartesian coordinate system is positioned so that the antenna starts in the origin and extends along the x axis with monopoles parallel to the (positive) z axis. The gray square represents a ground plane coinciding with the xy plane.

Based on the above, one unit cell is defined as a fraction of the antenna array containing one monopole and one measuring point. An N monopoles long array is hence equivalent to N unit cells lined up next to each other along the x axis.

4.1.2 Parameters

All geometrical parameters are scaled to fit a design frequency f_0 through the relations

$$d = \frac{\lambda_0}{4}\left(1 - \frac{1}{N}\right) \tag{4-1}$$

following the Hansen-Woodyard design where $\lambda_0 = c/f_0$ is the corresponding design wavelength and c is the speed of light in vacuum,

$$l = \frac{\lambda_0}{4} \tag{4-2}$$

as the array consists of monopoles, and the radius r of a monopole

$$r = \frac{\lambda_0}{100} \tag{4-3}$$

where the constant 100 is chosen according to the NEC2 manual [19].

The design frequency f_0 might or might not be the same as the excitation frequency f. The excitation frequency in its turn decides the wave number k,

$$k = \frac{2\pi}{\lambda} \tag{4-4}$$

where $\lambda = c/f$ is the excitation wavelength. The frequency difference β depends on both f and f_0 through the Hansen-Woodyard relation from chapter 3,

$$\beta = kd + \frac{2.94}{N}. \tag{4-5}$$

4.1.3 Test data

The test data consists of the simulated values of the electrical field in x and z direction, respectively, in a number of equally spaced points along the x axis (i.e. parallel with the antenna array, see figure 4.1). This choice of measuring points implies that the field will be constantly zero in y direction.

The design frequency is chosen to $f_0 = 10$ GHz, and for comparison a number of frequencies centred around f_0 are used. Note that the antenna remains optimised for the central frequency throughout the whole simulation – only the frequency difference β will change with the excitation frequency in accordance with formula (4-5). Keeping β constant will impose demands on the power supply to the antenna. How this is realised is not a topic of this report, and will not be further discussed.

Every simulation produces three sets of values for the electric field, corresponding to three different values of z_0. These points are at height $z_0 = 0$, $z_0 = l$ and $z_0 = 2l$, and are numbered 1, 2, 3. The electric field is correspondingly denoted, for example E_{z_2} for the field in z direction in point 2 or E_{x_3} for the x component at height $2l$.

Most of the theory on which the investigations presented in this report are based was developed for infinite structures, while the simulated antenna is strictly finite. Having a finite antenna gives rise to side effects on the edges that has to be handled separately, at once making the problem much more complicated. Instead of handling these side effects by introducing reflected waves, the outermost elements of each side of the antenna array are discarded once the calculations are done and not used in the further analysis. This simplification is justified by our question at hand; is there a part of the antenna that can be characterized as periodic with no or little influence of the edge elements and analysed using a representative unit cell?

In general, if nothing else is specified, 3 unit cells at each end of the antenna are discarded. In order to clearly distinguish between the whole setup of values from a simulation and the values used in the analysis (with the outermost values at each side removed) the first is denoted E and the latter q.

4.2 Simulation software

Throughout this project 4nec2, a license free software for Windows built on the second version of The Numerical Electromagnetics Code (NEC-2), was used for simulations. NEC-2 is an implementation of MoM for analysis of the electromagnetic response of a metal structure specified by the user. A general overview of MoM was presented in 2.3. This section briefly describes the special case for NEC-2; how wires and ground planes are discretized, limitations of the program and finally something about input and output. More about the theory can be found in [13] while the user's guide [19] gives a detailed description of all features and how to use them.

4.2.1 Wire and ground plane modelling

NEC-2 uses two types of integral equations, one for wires and one for surfaces. A wire is divided into a number of segments specified in the input file; each built up by a constant, a sine and a cosine giving a current I_j for segment j described as

$$I_j(s) = A_j + B_j \sin\left(k(s - s_j)\right) + C_j \cos\left(k(s - s_j)\right), \qquad |s - s_j| < \Delta_j/2 \tag{4-6}$$

where s_j is the coordinate at the centre of the segment and Δ_j denotes the segment length. A_j, B_j and C_j are unknown constants of which two are eliminated using local conditions after expanding the current in a sum of basis functions. The basis functions used are the Bessel functions $J_0(\dots)$ and $J_1(\dots)$. For the problem stated in this thesis these boundary conditions are either of the below:

a) The charge as well as the current is continuous at the junction between two segments,

$$\left.\frac{\partial I(s)}{\partial s}\right|_{s=s_j\pm\Delta_j/2} = \frac{Q_1^{\pm}}{\ln\left(\frac{2}{ka}\right)-\gamma}, \tag{4-7}$$

where Euler's constant $\gamma = 0.5772$, or

b) at free ends, relaxing the current flowing onto the end cap according to

$$I_j(s_j \pm \Delta_j/2) = \frac{\pm 1}{k}\frac{J_1(ka)}{J_0(ka)}\left.\frac{\partial I(s)}{\partial s}\right|_{s=s_j\pm\Delta_j/2}. \tag{4-8}$$

The matrix equation of MoM, described in section 2.3, is then used to calculate the last unknown for each segment.

The perfect conducting ground plane is not discretized by NEC. Instead, the image method from section 2.2.4 is used, replacing the ground plane with images of the currents above it.

4.2.2 Limitations

According to [13], there is no theoretical limit for how large structures that can be modelled and solved for using the integral approach implemented in NEC-2. Though, the matrix grows for every segment, calling for more space to store it and more computer power to solve the equations. The code has a history going back to the 70's, and as a result of this the code itself limits the maximum memory usage allowed. There are several executable files available, of which the largest in the current version allow 11 kB.

In order to get an accurate solution the segments must be sufficiently short in comparison with the wavelength λ. This minimum requirement is

$$l_s < \frac{\lambda}{10} \tag{4-9}$$

where l_s is the length of the segment, although the half of this is recommended. [19]. In this thesis a minimum of 5 segments are used for each monopole.

Of course it is preferred to simulate as large structures as possible – the more elements in the array the more periodic it will appear – but with the above restrictions the largest array of monopoles possible turned out to be 256 elements long (i.e. N=256).

4.2.3 Input and output

In order to perform a simulation, NEC-2 needs a set of input parameters describing the structure geometry, loads and electrical properties. These can either be provided by hand via the graphic user interface in 4nec2, or by structured text files, the latter being more efficient for large structures and therefore used in this thesis. All options are described in detail in the manual [19]; the following is a short description of the ones used in this thesis.

An input file is produced using a MATLAB script, given the design frequency, excitation frequency, number of dipole wires, number of segments on each wire and number and start value of the measuring points as input parameters. The geometry of the whole structure is then calculated and written to a text file as in the example in figure 4.2.

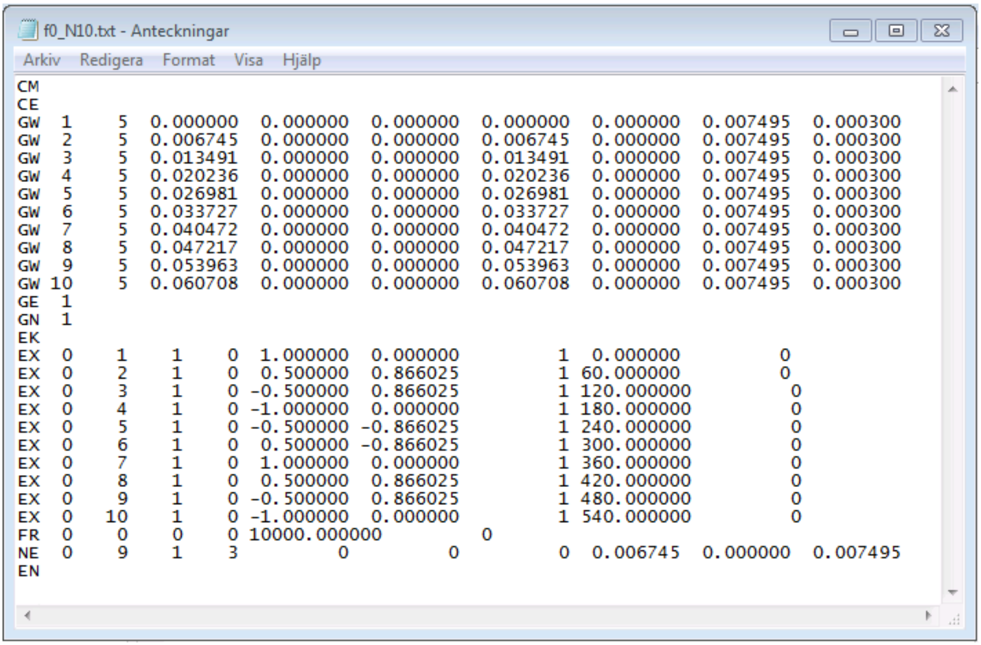
f0_N10.txt - Anteckningar
Arkiv Redigera Format Visa Hjälp

```
CM
CE
GW  1    5  0.000000  0.000000  0.000000  0.000000  0.000000  0.007495  0.000300
GW  2    5  0.006745  0.000000  0.000000  0.006745  0.000000  0.007495  0.000300
GW  3    5  0.013491  0.000000  0.000000  0.013491  0.000000  0.007495  0.000300
GW  4    5  0.020236  0.000000  0.000000  0.020236  0.000000  0.007495  0.000300
GW  5    5  0.026981  0.000000  0.000000  0.026981  0.000000  0.007495  0.000300
GW  6    5  0.033727  0.000000  0.000000  0.033727  0.000000  0.007495  0.000300
GW  7    5  0.040472  0.000000  0.000000  0.040472  0.000000  0.007495  0.000300
GW  8    5  0.047217  0.000000  0.000000  0.047217  0.000000  0.007495  0.000300
GW  9    5  0.053963  0.000000  0.000000  0.053963  0.000000  0.007495  0.000300
GW 10    5  0.060708  0.000000  0.000000  0.060708  0.000000  0.007495  0.000300
GE  1
GN  1
EK
EX  0    1    1    0  1.000000  0.000000        1   0.000000        0
EX  0    2    1    0  0.500000  0.866025        1  60.000000        0
EX  0    3    1    0 -0.500000  0.866025        1 120.000000        0
EX  0    4    1    0 -1.000000  0.000000        1 180.000000        0
EX  0    5    1    0 -0.500000 -0.866025        1 240.000000        0
EX  0    6    1    0  0.500000 -0.866025        1 300.000000        0
EX  0    7    1    0  1.000000  0.000000        1 360.000000        0
EX  0    8    1    0  0.500000  0.866025        1 420.000000        0
EX  0    9    1    0 -0.500000  0.866025        1 480.000000        0
EX  0   10    1    0 -1.000000  0.000000        1 540.000000        0
FR  0    0    0    0 10000.000000         0
NE  0    9    1    3         0         0        0  0.006745  0.000000  0.007495
EN
```

Figure 4.2 - An example input file to NEC.

Each line starts with two letters, cards, telling the program what could be found on that row. CM and CE marks start and end of comment lines to be ignored. A GW card is followed by a geometrical description of a wire, including tag number, number of segments, start and end points in x, y and z direction respectively, and in the last column the radius of the wire. The geometry description is terminated with GE followed by an integer flag describing the ground plane, in this case 1, which means a ground plane is present and segments touching it will be interpolated using image theory. GN specifies the ground plane, 1 meaning perfectly conducting ground, and EK is a flag to control that the extended thin-wire kernel approximation is used for computation.

Next follows a number of excitation cards, EX, with specifications for source type (in this case 0 indicating a voltage source), tag number, segment number, real and imaginary parts of the voltage source, magnitude and phase. FR is the frequency specification. NE requests the near electric field to be computed as specified on that line, with number of measuring points, starting point and step length in x, y and z direction, respectively. The last row contains the end of data flag, EN, ending all program execution.

In a real application, every element would also have a load parallel to the source. This can be simulated in NEC using the LD card, but since none of the investigations in this thesis requires information about the loads they are not included in this model.

Running the simulation generates an output file, which is quite extensive in comparison to the input. Not all data is used for the analysis, and figure 4.3 shows only the near electric fields part of the example output file (the one generated using the example input file in figure 4.2).

f0_N10.out.txt - Anteckningar

Arkiv Redigera Format Visa Hjälp

```
                                   - - - NEAR ELECTRIC FIELDS - - -

        -  LOCATION  -                        -  EX  -                 -  EY  -                 -  EZ  -
    X           Y           Z          MAGNITUDE   PHASE        MAGNITUDE   PHASE        MAGNITUDE   PHASE
  METERS      METERS      METERS        VOLTS/M   DEGREES        VOLTS/M   DEGREES        VOLTS/M   DEGREES
   0.0000      0.0000      0.0000     0.0000E+00     0.00      0.0000E+00     0.00      7.2583E+02   180.00
   0.0067      0.0000      0.0000     0.0000E+00     0.00      0.0000E+00     0.00      7.2589E+02  -120.02
   0.0135      0.0000      0.0000     0.0000E+00     0.00      0.0000E+00     0.00      7.2585E+02   -60.02
   0.0202      0.0000      0.0000     0.0000E+00     0.00      0.0000E+00     0.00      7.2586E+02    -0.02
   0.0270      0.0000      0.0000     0.0000E+00     0.00      0.0000E+00     0.00      7.2585E+02    59.98
   0.0337      0.0000      0.0000     0.0000E+00     0.00      0.0000E+00     0.00      7.2584E+02   119.98
   0.0405      0.0000      0.0000     0.0000E+00     0.00      0.0000E+00     0.00      7.2583E+02   179.98
   0.0472      0.0000      0.0000     0.0000E+00     0.00      0.0000E+00     0.00      7.2582E+02  -120.02
   0.0540      0.0000      0.0000     0.0000E+00     0.00      0.0000E+00     0.00      7.2580E+02   -60.03
   0.0000      0.0000      0.0075     7.4117E+01   131.53      0.0000E+00     0.00      1.3468E+03  -137.98
   0.0067      0.0000      0.0075     9.5029E+01  -158.23      0.0000E+00     0.00      1.5672E+03   -53.75
   0.0135      0.0000      0.0075     9.9573E+01   -98.57      0.0000E+00     0.00      1.5046E+03     3.78
   0.0202      0.0000      0.0075     9.8066E+01   -40.97      0.0000E+00     0.00      1.4609E+03    65.00
   0.0270      0.0000      0.0075     9.3499E+01    18.28      0.0000E+00     0.00      1.4445E+03   123.31
   0.0337      0.0000      0.0075     9.5415E+01    71.33      0.0000E+00     0.00      1.3944E+03  -178.81
   0.0405      0.0000      0.0075     9.4459E+01   126.54      0.0000E+00     0.00      1.3965E+03  -121.91
   0.0472      0.0000      0.0075     9.8502E+01  -179.53      0.0000E+00     0.00      1.4421E+03   -67.38
   0.0540      0.0000      0.0075     1.2540E+02  -133.83      0.0000E+00     0.00      1.6347E+03   -13.16
   0.0000      0.0000      0.0150     6.0343E+01    92.71      0.0000E+00     0.00      8.6934E+01   129.36
   0.0067      0.0000      0.0150     6.8722E+01   158.43      0.0000E+00     0.00      9.1762E+01  -170.28
   0.0135      0.0000      0.0150     7.1087E+01  -143.93      0.0000E+00     0.00      9.1861E+01  -105.88
   0.0202      0.0000      0.0150     6.8329E+01   -85.90      0.0000E+00     0.00      9.4365E+01   -44.53
   0.0270      0.0000      0.0150     6.6122E+01   -26.16      0.0000E+00     0.00      9.0311E+01    17.42
   0.0337      0.0000      0.0150     6.5276E+01    31.85      0.0000E+00     0.00      8.7432E+01    81.53
   0.0405      0.0000      0.0150     6.2786E+01    88.31      0.0000E+00     0.00      8.2368E+01   144.30
   0.0472      0.0000      0.0150     5.9088E+01   143.40      0.0000E+00     0.00      7.3385E+01  -150.10
   0.0540      0.0000      0.0150     4.8131E+01  -166.82      0.0000E+00     0.00      6.6494E+01   -82.02



***** DATA CARD NO. 15   EN   0     0     0     0  0.00000E+00  0.00000E+00  0.00000E+00  0.00000E+00  0.0000(

RUN TIME =      0.047
```

Figure 4.3 - Parts of an example output file from NEC.

The output file starts by repeating the geometrical input, and then follows the resulting segmentation data describing how the structure was divided into smaller parts for analysis. Hereafter comes the excitation and frequency information along with calculated voltage, current, impedance, admittance and power at the first segment of each monopole antenna. The next section is called currents and locations and displays geometrical properties in units of wavelength as well as currents for every segment. Depicted in figure 4.3 is the last part of the input file containing the values used for analysis in this thesis, location of the measuring points and near electric fields in x, y and z direction for the three different heights over the ground plane chosen, respectively.

4.3 Hypotheses

Finding plausible hypotheses describing the electric field from an endfire antenna is an evolving process of testing, rejecting, developing and testing again; some ideas turning out to be dead-ends and some worth a closer look. Of course all of this work could not be included in this report. Instead, hypotheses of special interest were selected and are presented in the following subsections.

First, the NEC simulation is compared to the result when assuming no coupling between the elements. Then, three hypotheses are tested. The first one is really simple; assuming that an active periodic structure is nothing different from a passive one. The following two are based on the first with slight changes due to the results of the simulations. All three hypotheses have separate sections in the result chapter, and the reader may reach a better understanding by skipping ahead to the results for one hypothesis before moving on to the next.

4.3.1 Coupling between elements

Before starting out with more advanced investigations, it is a good idea to check how close to the true field value a calculation assuming no coupling between the monopoles can come. This assumption leads to easy calculations, as the monopoles can be treated as independent antennas which through superposition sums up to the total electric field around the structure. Using image theory to treat the ground plane, the problem is equal to an array of dipoles. Each has an $\boldsymbol{E}$ field according to formula 2-27a and the field in one measuring point is the sum of the separate fields from all dipoles.

4.3.2 Passive periodic structure

A plausible starting point for further investigations to build on would be to address the most fundamental and important question to be answered: Is there any significant difference to the case of a passive periodic structure? If there is no difference, the well-developed theory for passive periodic structures can be directly applied.

Thus, as a first naive hypothesis, the expression for the electric field in a passive periodic structure,

$$E(x+nd) = E(x)e^{-j\beta nd}, \tag{4-10}$$

is adopted. With the intention to enable a simple first analysis, the propagation constant β is assumed to be real in this case.

4.3.3 Complex propagation constant

In this section the first hypothesis is extended to include a possibility for the propagation constant to be a complex number with both a real and an imaginary part. This more general form is written using the Bloch wave number $K = -j\alpha + \beta$ as

$$E(x + nd) = E(x)e^{-jKnd} = E(x)e^{-j(-\alpha j+\beta)nd}. \qquad (4\text{-}11)$$

Note that the β in the above formula is not the same as in the previous section; it is just the denotation for the real part. Determination of both the imaginary and the real part, α and β, of the Bloch wave number calls for more complex methods, and the primary interest in a first stage here is to find whether there is an imaginary part, or not. Analysis of this hypothesis will therefore be focused on the possible existence of this imaginary part α.

4.3.4 Polynomial factor

Considering the results in section 5.2 after investigating the hypothesis in section 4.3.2, one notices a remaining amplitude increment or decrement (depending on the height z_0 over the ground plane of the measuring points) of the electric field at the end of the antenna that is not picked up by the simple model. An attempt to pick up this increment is to multiply the expression with a polynomial in n,

$$E(x + nd) = E(x)e^{j\varphi n} \cdot (b_1 + b_2 n + b_3 n^2 + \cdots) \qquad (4\text{-}12)$$

where b_1, b_2 ... are real constants and φ collects the frequency content.

4.4 Analysis outline

4.4.1 Coupling between elements

Instead of using formula 2-27a directly in the summation, a simplified form without all the constants,

$$\boldsymbol{E}(\boldsymbol{r}) = \sum_{n=1}^{N} \frac{e^{-jk|r-r'_n|}}{|r-r'_n|} e^{-j\varphi n} \widehat{\boldsymbol{\theta}}(\boldsymbol{r}, \boldsymbol{r}'_{\boldsymbol{n}}), \qquad (4\text{-}13)$$

is used. Here $\boldsymbol{r}$ is the measuring point, $\boldsymbol{r}'$ is the source point, k is the wave number, φ is the phase difference and n is the element number. The notation $\widehat{\boldsymbol{\theta}}(\boldsymbol{r}, \boldsymbol{r}_n)$ means that $\widehat{\boldsymbol{\theta}}$ is different for each source-measuring point pair, and the z and x components are summarised separately. What in fact is calculated with this formula is the array factor, assuming $\theta = 90°$. This is a good approximation at some distance from the source, but worse for measuring points near the considered monopole.

Using MATLAB, two arrays are constructed and the z components of their respective electric fields are calculated. The first is a Hansen-Woodyard design just like the one in the problem description, the second with the dipoles further apart at a distance $d = \lambda$ for comparison. The same calculations are done using NEC-2. Comparing the results, there will be a good compliance between the two methods for the array with the larger distance between the elements and a greater difference for the Hansen-Woodyard array if coupling exists.

To allow the point dipole approximation in the MATLAB case to be compared to the half-wave dipole in the NEC case the measurements must be made at some distance (order of wavelengths) above the ground plane. Also, the values must be normalised since the difference otherwise will depend on the removed constants in the first case.

4.4.2 Passive periodic structure

This hypothesis can easily be examined using the well-known fact that taking the logarithm of a constant multiplied with a purely exponential expression results in another constant multiplied with the expression in the exponent. First, to get a cleaner look, a is defined as the constant part of the exponential,

$$q(n) = q(1)e^{-j\beta(n-1)d} = q(1)a^{(n-1)}. \tag{4-14}$$

Taking the logarithm gives

$$\ln\left(q(1)a^{(n-1)}\right) = (n-1) \cdot \ln\left(q(1)\right) \tag{4-15}$$

which in this case is a linear function. Thus, if this simple hypothesis holds up, plotting the absolute value of the electric field in a logarithmic scale plot should give rise to a straight line.

4.4.3 Complex propagation constant

As mentioned, to find the Bloch wave number K is a tricky task since both its imaginary and real part must be determined; two unknowns and one equation. Luckily, there is a reasonably simple way to find the imaginary part, as its (possible) existence constitutes the most essential part of this analysis. To begin with, the constant part of the exponent is rewritten in the same manner as before,

$$q(n) = q(1)e^{-jK(n-1)d} = q(1)a^{(n-1)} \tag{4-16}$$

and then follows an expansion using the Z-transform described in detail in [20],

$$X(z) = \sum_{k=-\infty}^{+\infty} x_k z^{-k}, \tag{4-17}$$

where $X(z)$ is the Z-transform of the sequence x_k. Applying this to q, defining $Q(z)$ as its Z-transform, results in

$$Q(z) = \sum_{n=1}^{N} q(n)z^{-(n-1)} = q(1)\sum_{n=2}^{N} \left(\frac{a}{z}\right)^{(n-1)}. \tag{4-18}$$

If the upper summation limit had been infinity, the corresponding series would be convergent if and only if $|a/z| \le 1$ which leads to

$$|z| = |a| = |e^{-j(\beta+j\alpha)d}| = e^{\alpha d} \tag{4-19}$$

for the convergence limit and, since d is known, thereby allows us to calculate α by finding the value of z for which the series converge. The absolute value of $Q(z)$ is calculated as the sum of the absolute values in the summation symbol,

$$|Q(z)| = \sum_{n=1}^{N} \left|q(n)z^{-(n-1)}\right|. \tag{4-20}$$

The coupling between the radius of convergence and the corresponding value of z is illustrated in figure 4.4. The darker grey strip in the bottom picture marks the area enclosing the border of the convergence interval; above in the almost white grey area |Q(z)| certainly diverges and in the lower light grey area it certainly converges. Correspondingly, in the upper picture the darker grey circle encloses the circular border of the outer convergence area. The requirement $|a| = |z|$ is fulfilled somewhere between the horizontal lines. If $|z| \neq 1$, a nonzero imaginary part of K exists and can be determined.

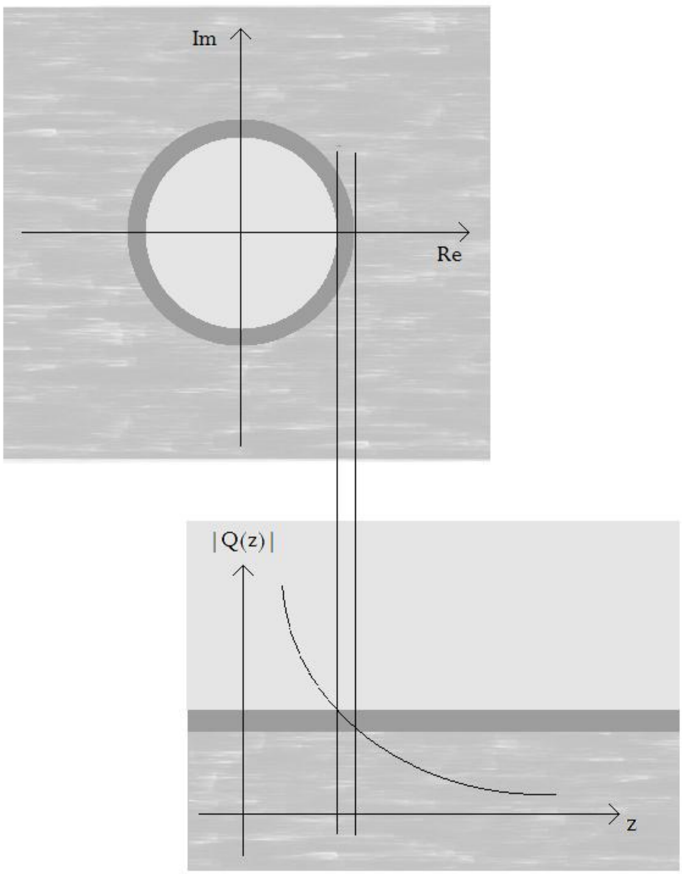

Figure 4.4 - Coupling between the radius of convergence for the Z transform and the corresponding value of z.

Before moving on one big question arises that has to be treated: Where do we draw the line between convergence and divergence in a given plot? Is it when the sum exceeds a certain predetermined value, when the absolute value of the derivative becomes really large or when the growth of the curve is super-exponential? The arbitrariness in the choice of this boundary could indeed affect the outcome a lot, and therefore the analysis includes varying this boundary and comparing the results before any conclusion is drawn.

4.4.4 Polynomial factor

The idea here is to divide all measured values in the left hand vector in formula 4-12 with the first value and the exponent part of the right hand expression, leaving only the polynomial.

$$\frac{q_n}{q_1 \cdot e^{\varphi j n}} = (b_1 + b_2 n + b_3 n^2 + \cdots) \qquad (4\text{-}21)$$

Step one is to determine the frequency content φ. This is done using the Fast Fourier Transform (FFT) technique. The whole vector of values, q, is transformed along with three different discrete sinus functions of different frequencies used as references. These references are needed since the FFT function in MATLAB determines the frequency in units of vector length, meaning that the frequencies for a vector of length N is given in the interval $[0, N]$. By fitting a line to the known reference values using the built-in MATLAB polyfit function the frequency content of q is calculated. Figure 4.5 shows the FFT of the reference functions (dotted) and q (solid) respectively. FFT generates both positive and negative frequencies, which is the reason for the double set of peaks for the sine functions. The positive peaks are the ones of interest.

Once φ is known the left-hand side of equation 4-21 can be determined. This vector is a point representation of the polynomial in the right hand side of equation 4-21, and the goal is to find a line that fits.

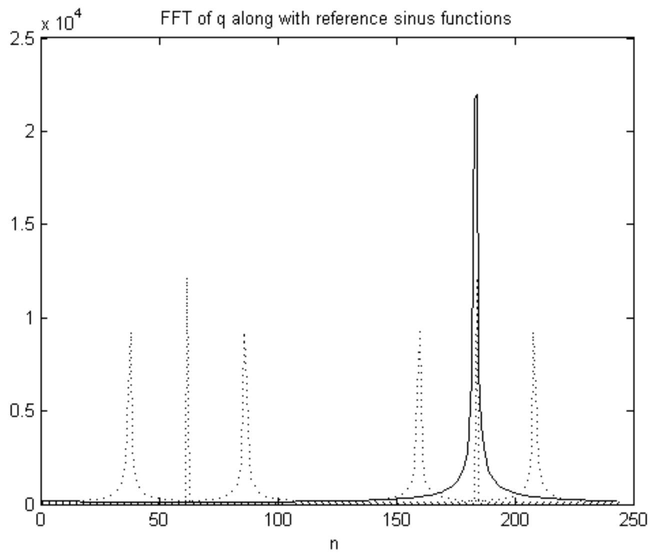

Figure 4.5 - FFT for q (solid line) and reference sinus functions (dotted lines) used to calculate the frequency content φ.

5

5 Results with discussion

In this chapter the results are presented in figures, tables and explaining text. Each result is briefly discussed directly after it has been presented to reflect the way of working during this thesis project. The last section contains a more general discussion that summarises the work.

5.1 Coupling between elements

Results from the MATLAB as well as the NEC calculations for the two arrays are found in figure 5.1. The top graphs show the normalized values for the x component of the electric field and the bottom graphs show the corresponding values for the z component. Left is the Hansen-Woodyard design and to the right is the $d = \lambda$ design. The measuring points, in this case, were at a height 2λ over the ground plane.

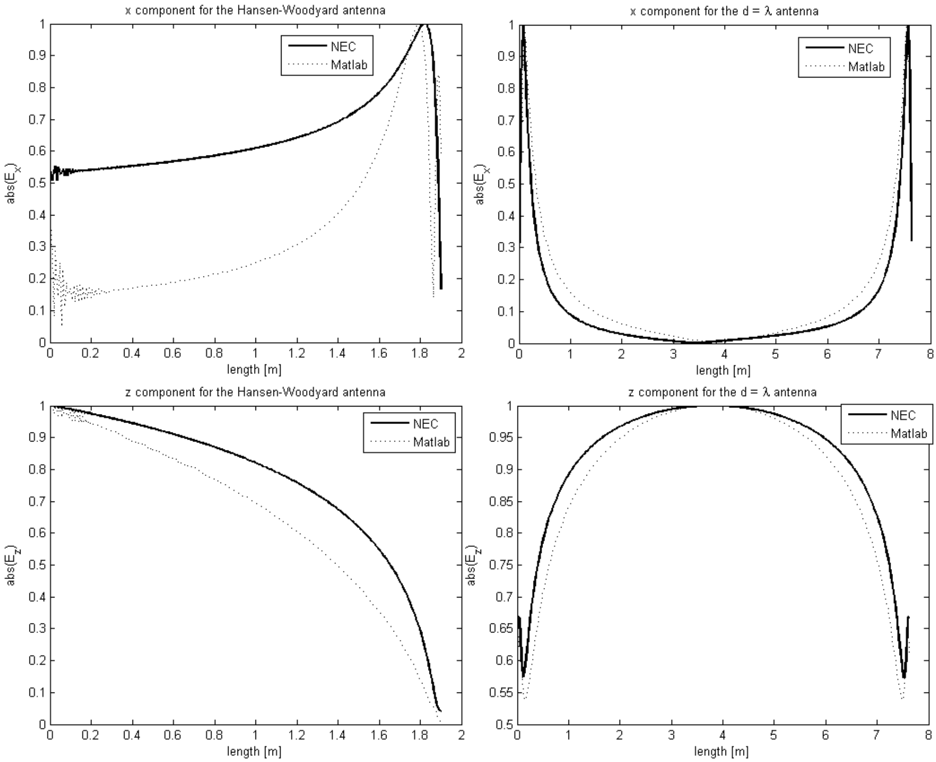

Figure 5.1 - Comparison between NEC simulation and Matlab far field calculation of the electric field for a HWEA (left graphs) and a $d = \lambda$ antenna (right graphs). The top graphs show the x component and the bottom two shows the z component.

As seen in the picture, the results for the Hansen-Woodyard array, especially for the x component, differ significantly more than for the $d = \lambda$ array. Tests with larger distances between the elements in the latter case, implying even less coupling, as well as measurements higher above the ground plane, reducing the influence of the half-wave versus point dipole dissimilarity, results in an even larger difference between the two setups. Thus, the coupling between the elements can not be neglected.

5.2 Passive periodic structure

Figure 5.2 and 5.3 are the plots of the absolute value of the electric field along an antenna array with $N = 256$ for four different excitation frequencies. Figure 5.3 contains three plots corresponding to E_{z_1}, E_{z_2} and E_{z_3}, respectively. Figure 5.2

holds only two plots, the upper for E_{x_3} and the lower for E_{x_2}, since the $\boldsymbol{E}$-field in x direction at the ground plane always will be zero and is therefore of no interest here.

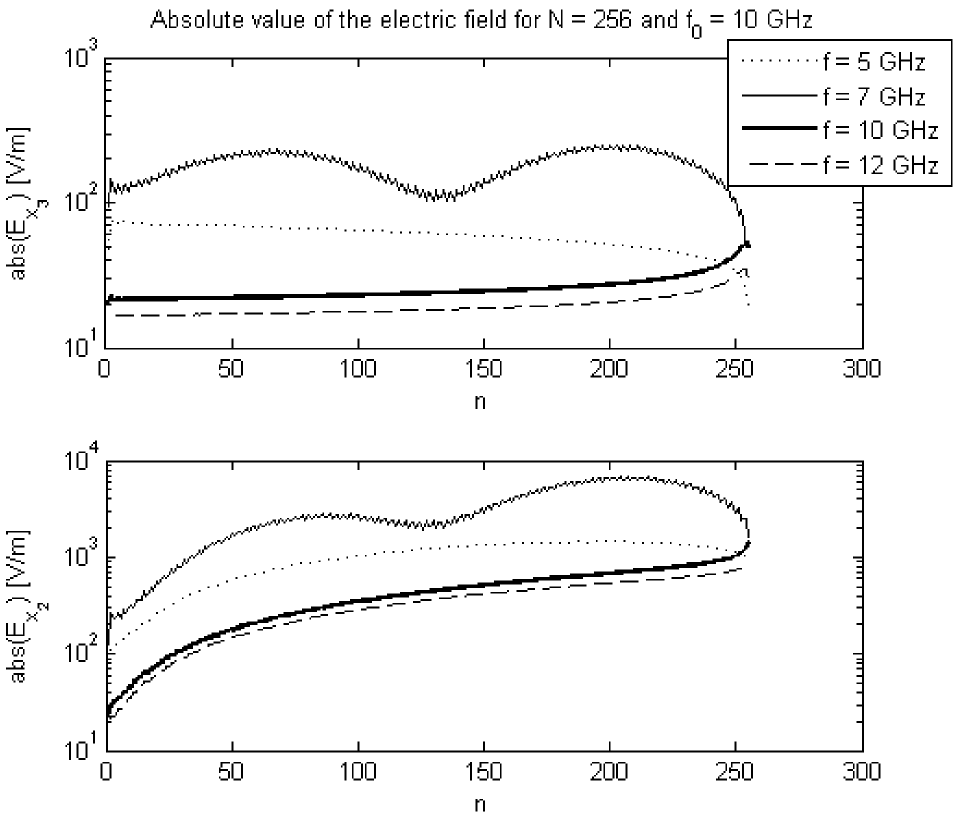

Figure 5.2 - Logarithmic scaled plots of the absolute value of the x component of the electric field over a HWEA with N = 256 and f_0= 10 GHz at four different excitation frequencies at two different heights over the ground plane.

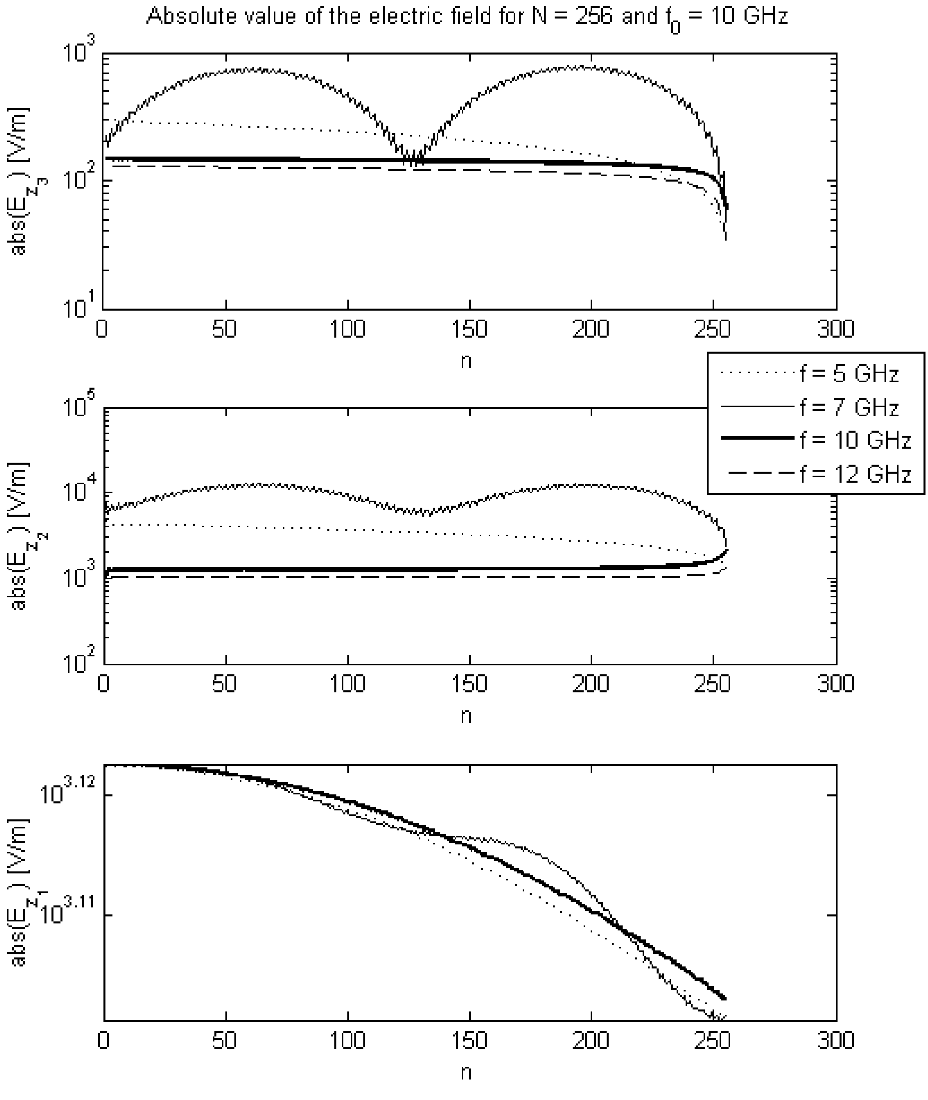

Figure 5.3 - Logarithmic scaled plots of the absolute value of the z component of the electric field over a HWEA with N = 256 and f_0= 10 GHz at four different frequencies at three different heights over the ground plane.

Looking at the plots, the first thing to notice is that none of them depict straight lines, and thus the hypothesis that an active periodic structure is nothing different from a passive ditto is proved to be false. With this conclusion made, a new, refined hypothesis is needed, and in order to find one, so is a deeper analysis.

Except for the 7 GHz curve, common to the different frequencies concerning the z component, is that the values in the left part of the figure follow a fairly straight line (note the scale of the y axis for the E_{z_3} plot), whereas the right end has either a dip or a rise. The same holds for E_{x_3}, but E_{x_2} is different with a dip at the left side as well. The fact that part of the curve is straight implies that equation 4-10 after all is a fairly good approximation for part of the structure, especially for the z component, but it needs to be modified in some way. A good way to start could be to relax the assumption of a real propagation constant and letting it be complex.

Whether the curve bends up or down seems to depend on both frequency and height over the ground plane. Worth noticing is also that 5 GHz and 7 GHz gives higher values than the design frequency 10 GHz. The small oscillations in the 5 GHz and 7 GHz curves is due to inter-cell variations, which will be seen further on.

Before moving on, the 7 GHz interference phenomenon is worth a closer look. Simulations from 1 GHz up to 9 GHz with 1 GHz steps show that only 7 GHz and 8 GHz interfere; the rest have the same form as the design frequency. Additional simulations were performed to find the interference interval, and the results for E_{z_3} can be found in figures 5.4 and 5.5 below.

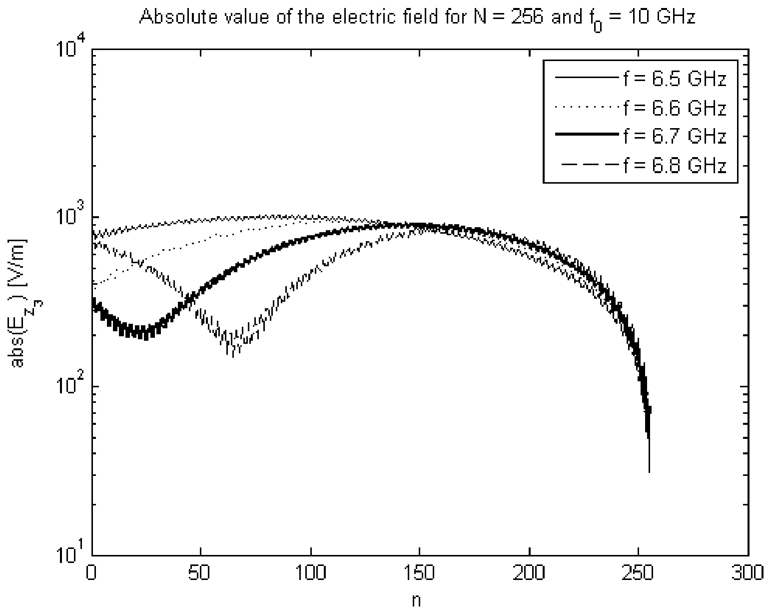

Figure 5.4 - The absolute value of the electrical field for excitation frequencies at the lower boundary of the interfering interval.

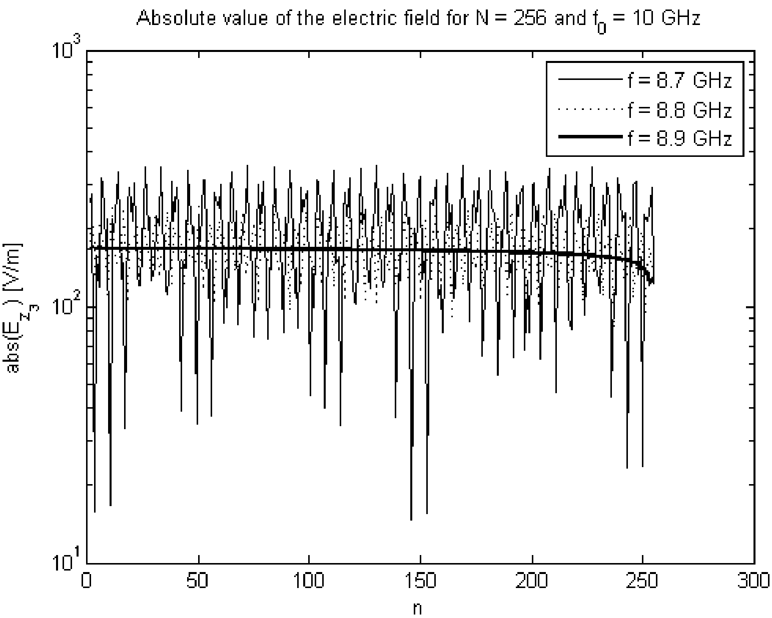

Figure 5.5 - The absolute value of the electrical field for excitation frequencies at the higher boundary of the interfering interval.

Figure 5.4 shows that the interference starts around 6.6 GHz, and from figure 5.5 it can be seen that there is still interference at 8.8 GHz while 8.9 GHz again looks like the non-interfering frequencies.

In this context, it would be interesting to vary the edge elements in order to get an idea of how they affect the centre part of the array. In figure 5.6 the distance d_e between the edge elements is varied, and in figure 5.7 the length of the edge elements, l_e, is set to a different value than for the centre elements. As inspiration for deciding the magnitude of these changes, the Yagi-Uda antenna described in [6] is used. In that case, the edge elements has length $l_e \sim 0.9l$ and a distance $d_e \sim 0.8d_0$.

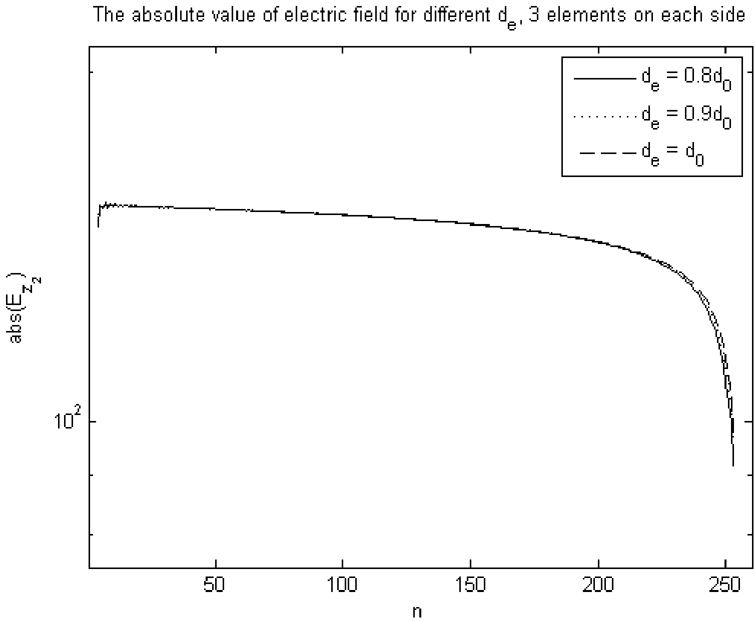

Figure 5.6 - The absolute value of the electric field with different values of d_e for the 3 outermost elements on each side of the antenna array.

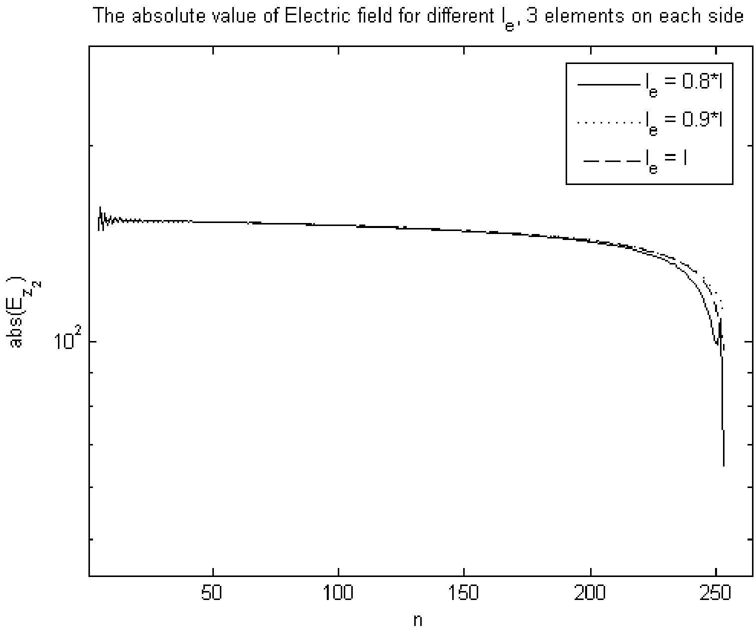

Figure 5.7 - The absolute value of the electric field with different values of l_e for the 3 outermost elements on each side of the antenna array.

In the figures above, the edge elements are not part of the plot. One first observation is thus that altering the edge elements does indeed affect the inner part of the antenna. Initially there is an oscillation, and in the right end the bend of the curve is slightly different. Still, in both cases, there is a part of the antenna for which the changes has very little (if any) effect, implying that this part can be treated as periodic.

Finally, the edge effects are studied in more detail by taking 20 measuring points in each unit cell to capture any inter-cell variations. Figure 5.8 shows the results for three different frequencies with and without changing the edge elements.

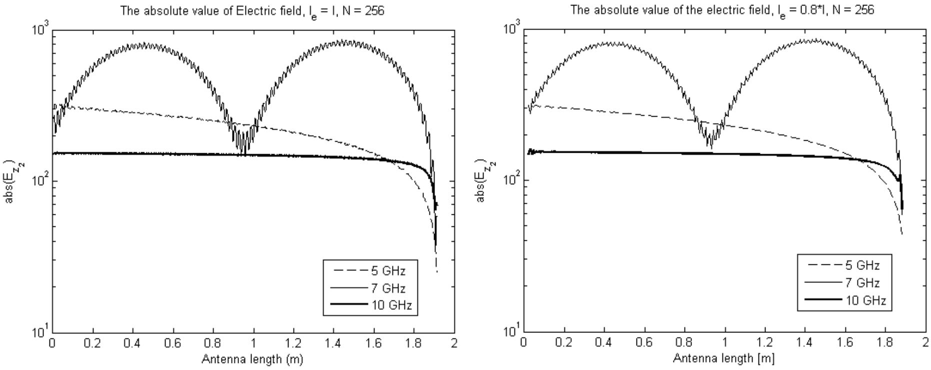

Figure 5.8 - The absolute value of the electric field with 20 measuring points in each element for three different excitation frequencies and $l_e = l$ (left), and $l_e = 0.8l$ (right).

The period of the oscillations that is seen when having multiple measuring points in each unit cell is the same for all frequencies, one per unit cell, and corresponds to the inter-cell variations that is present for all frequencies. The main difference when changing the edge elements as done in the right figure is that the magnitude of the inter-cell variations becomes smaller, and for 10 GHz they disappear almost entirely.

5.3 Complex propagation constant

Recalling from the method part, the goal was to find the value of z where the Z-transform series starts to converge, fulfilling $|z| = |a|$. The resulting plot of z versus $|Q(z)|$ for $f = f_0 = 10$ GHz and for three different values of N can be found in figure 5.9 below. The plot starts in $z = 0.98$, since the sum diverge strongly for lower values, and illustrates the values obtained for E_{z_3}. The results are normalized with N in order to compensate for that the total number of terms differs between the sums.

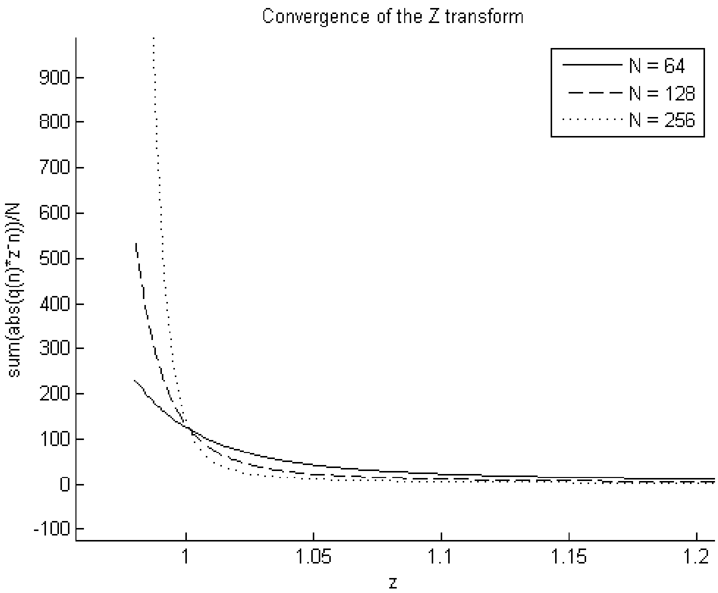

Figure 5.9 - The sum of the Z transform as function of z value for three different *N*.

The intersection at $z \approx 1$ is in fact three intersections laying close to each other, one between each pair of lines. As mentioned, the tricky part here is to set the limit for where the sum goes from divergent to convergent. This difficulty is evident in the figure, where it also is indicated that the value might not be the same for all N. In an attempt to avoid total arbitrariness in this choice a number of different sum value limits are tested and compared. For this purpose, a set of plots with scales adjusted to fit each of the lines in figure 5.9 are used, see figure 5.10. Table 5.1 lists the results for nine limit values v for each plot; the corresponding z and the differential $\frac{\Delta v}{\Delta z}$ as a measurement of how much z changes with the choice of v. The values picked are measure points as close to 20, 40, 60, 80, 100, 120, 140, 160 and 180 as possible for each N.

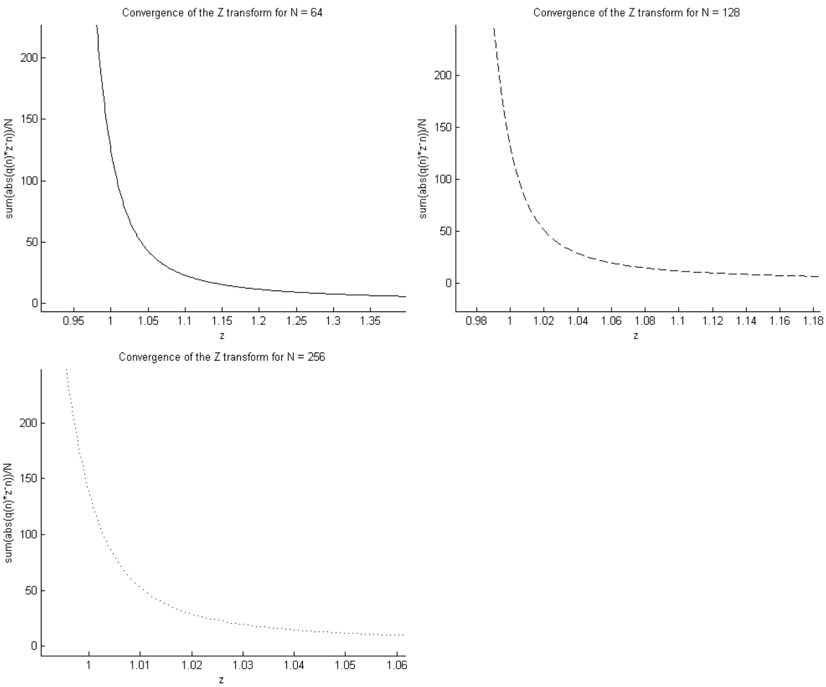

Figure 5.10 - Graphs used to pick out the values in table 5.1.

v			z			$\Delta v/\Delta z$		
64	**128**	**256**	**64**	**128**	**256**	**64**	**128**	**256**
20.02	19.84	20.04	1.116	1.058	1.029	—	—	—
40.21	40.37	39.8	1.054	1.027	1.014	325.6	662.3	1317
59.9	59.82	61.32	1.031	1.016	1.008	856.1	1768	3587
80.8	81.55	80.24	1.017	1.009	1.005	1493	3104	6307
100.6	99.75	98.22	1.008	1.005	1.003	2200	4550	8990
121.1	117.5	122.6	1.001	1.002	1.001	2929	5917	12190
139.5	139.9	138	0.996	0.999	1	3680	7467	15400
161.9	158.1	156.2	0.991	0.997	0.999	4480	9100	18200
177.6	179.6	177.7	0.988	0.995	0.998	5233	10750	21500

Table 5.1 - Values for the Z transform for N = 64, 128 and 256, respectively.

From the table it can be observed that $\Delta v/\Delta z$ in a point is doubled when N is doubled. Around $v = 120$ the value of z is almost the same for all three array lengths N; this is the intersection in figure 5.9.

It is hard to conclude anything from table 5.1 since the limit seems to lie around $z = 1$, the value for which

$$\alpha = \ln|z|/d = 0$$

and the propagation constant is real. Thus, there is a possibility that it is real, but it could as well be complex.

What could be said, though, is that the curve is steeper for larger N, and thus the interval enclosing the convergence limit gets narrower as N increases. Still, $z = 1$ can not be considered as not being part of this interval. The results can thereby not be used to falsify the hypothesis that K is real.

5.4 Polynomial factor

The result from this analysis aims to answer a two-part question; can the electric field over the endfire antenna be modelled by an exponential multiplied with a polynomial in n, and if so, how many terms are needed to get a sufficient compliance? Polynomials were fitted both to the original, complex-valued remainder, i.e. the left hand side of formula 4-21, and to the absolute value thereof, respectively. As both polynomials show similar behaviour, while the latter has real coefficients which are more suitable when it comes to visualisation in a plot, the presented results are for the absolute value.

Figure 5.11 shows the remainder and fitted polynomials of degree 2, 3 and 4 for an antenna with $f = f_0$ and $N = 256$. The results are similar for choices of f that is not interfering, i.e. except for the interval bounded by the frequencies in figures 5.4 and 5.5.

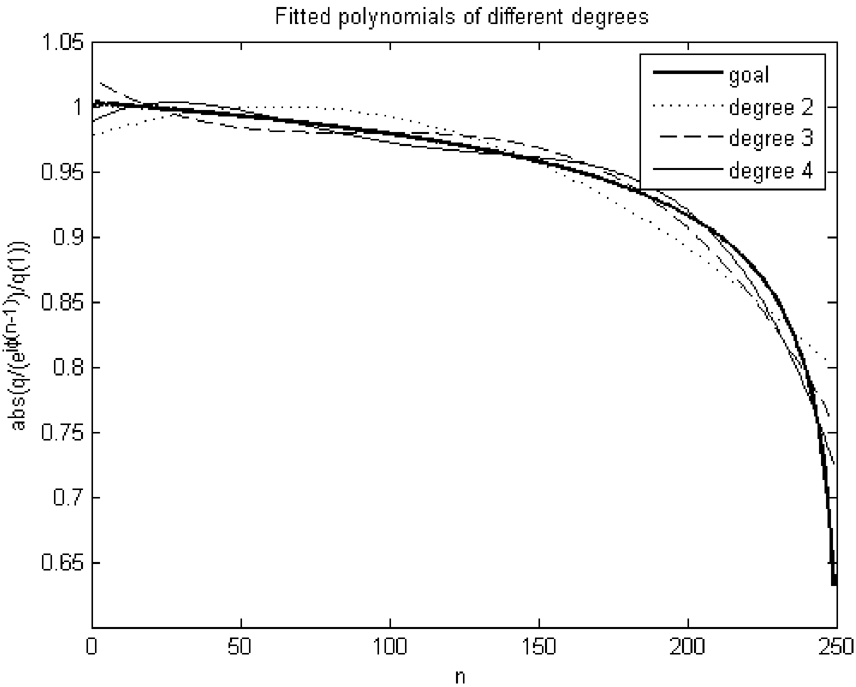

Figure 5.11 - Remainder along with fitted polynomials of degree 2, 3 and 4.

Especially in the rightmost part of the plot, there is a significant difference between the polynomials and the actual remainder, the "goal". This means that the bend is too steep to be picked up by a polynomial, and can not be included in the part of the antenna treated as periodic in this model. Dividing the remainder with the fitted polynomials should give the value 1 for all n for a perfect fit. This has been done in figure 5.12 to get a visually clearer image showing that it is the steep bend that causes the problem here.

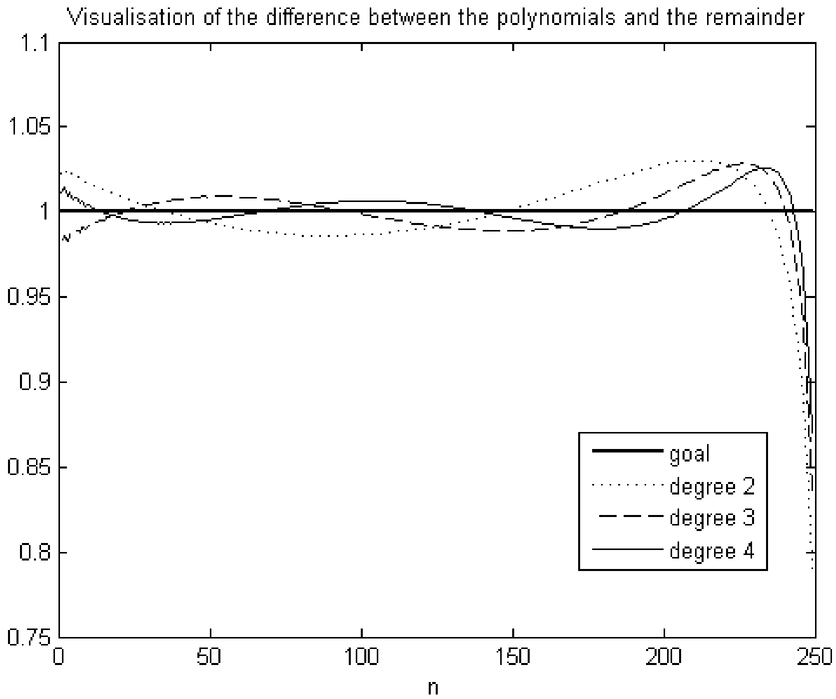

Figure 5.12 - Relative difference between the reminder and the three fitted polynomials.

The model is for a periodic structure, and of the values used to produce the above images, only 3 of the measured points at each side where removed. This is most likely not enough to eliminate the effect of the edge elements. In order to investigate if there is a part of the antenna that can be treated as periodical with the suggested model, the analysis was remade with 10, 20, 30 and 40 values at each side removed. Results are presented in figure 5.13, in the same manner as in 5.12.

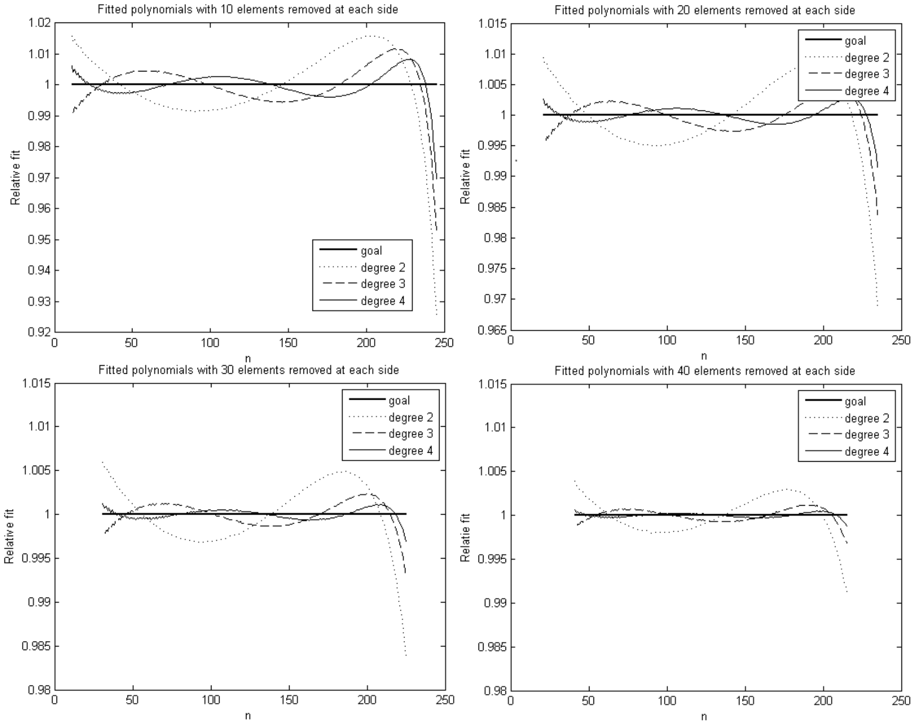

Figure 5.13 - Relative difference between the remainder and the fitted polynomials with 10, 20, 30 and 40 elements removed from each side, respectively.

With more values removed, the polynomials do not differ as much from the remainder. Still, the largest relative deviation remains in the right end of the array. Table 5.2 contains numerical values for the largest deviation for each of the cases in per polynomial degree.

Elements removed /polynomial degree	**10**	**20**	**30**	**40**
2	7.48 %	3.14 %	1.16 %	0.87 %
3	4.77 %	1.62 %	0.70 %	0.32 %
4	3.02 %	0.84 %	0.31 %	0.12 %

Table 5.2 - Largest deviation in percentage for each of the cases in figure 5.13.

Removing more elements decreases the deviation more than increasing the polynomial degree one step between 10 and 20 as well as between 20 and 30.

Between 30 and 40 both methods give approximately the same improvement. Where to draw the line for what is an acceptable deviation is up to the user, but as N influences the result as much as it does implies that more elements may have to be removed in order to get a nice fit with the proposed model.

One way to determine whereas the polynomial fit is a good method is to look at how the coefficients change with increasing polynomial degree; the more stable coefficients, the better. Table 5.3 shows coefficients for an array with $N = 256$ and $f = f_0$ and 30 elements removed at each side. In order to get coefficients of approximately the same magnitude, the array is centred on the origin and scaled so that $n \in [1, -1]$.

Coefficient /polynomial degree	$\boldsymbol{b_0}$	$\boldsymbol{b_1}$	$\boldsymbol{b_2}$
2	0.9730	-0.0506	-0.0295
3	0.9730	-0.0381	-0.0295
4	0.9716	-0.0381	-0.0160

Table 5.3 - Coefficients of the fitted polynomials of degree 2, 3 and 4 to an N = 256 array at 10 GHz.

The first coefficient, b_0, is almost the same for all three cases; it differs at the third digit between degree 3 and 4. The following two, b_1 and b_2, differs more, at worst almost a factor 2. As before, the results are similar for other choices of excitation frequency, except for the interfering ones. Higher degree polynomials were tested, but resulted in a "polynomial is bad conditioned" warning from the algorithm and was therefore discarded.

The second part of the two-part question was about how the coefficients could be calculated in advance, in order to be used in the simulation. So which parameters do they depend on and how? Figure 5.14 shows the dependency on N for a third degree polynomial when 3 values are removed at each side.

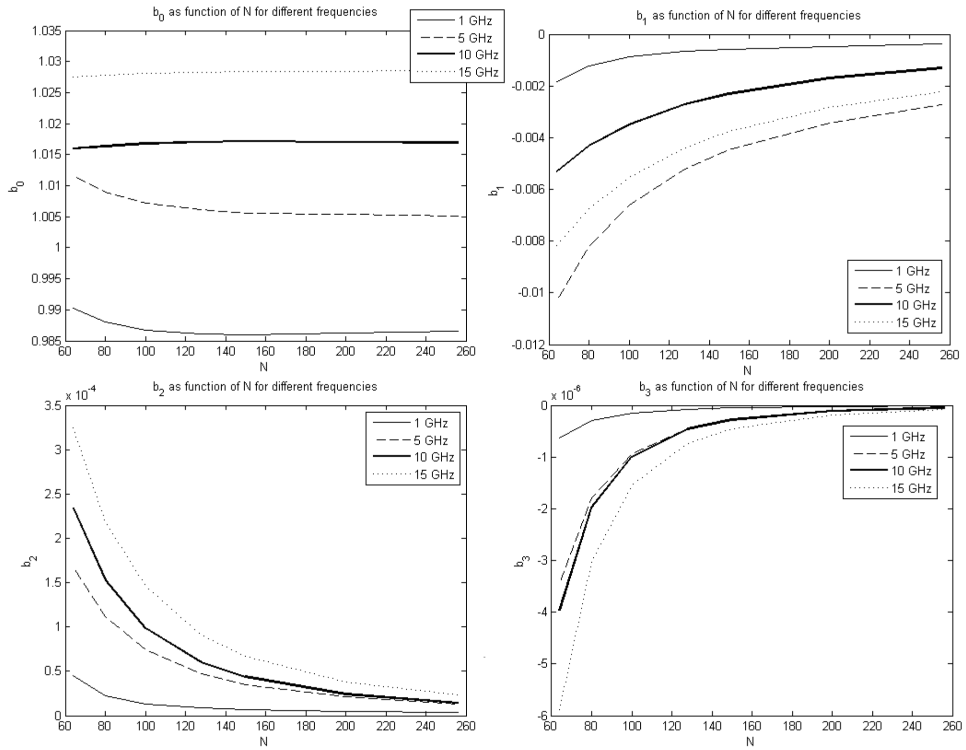

Figure 5.14 - The coefficients in a 3 degree polynomial as function of N. Upper left for b_0, upper right for b_1, lower left for b_2 and lower right for b_3.

It can be concluded from the graphs that the coefficients depend both on N and f. For larger N, they seem to asymptotically approach some value. For b_0, this value is clearly different for different frequencies, whilst for b_1, b_2 and b_3 no conclusion can be drawn from the results presented here. The lines corresponding to the different frequencies do not come in the same order in all plots, and the same random behaviour appears when plotting the coefficients as a function of excitation frequency.

The dependence on N becomes clear also in figure 5.15, where the reminder is plotted against n/N in order to compare the shape of the curve for different antenna lengths.

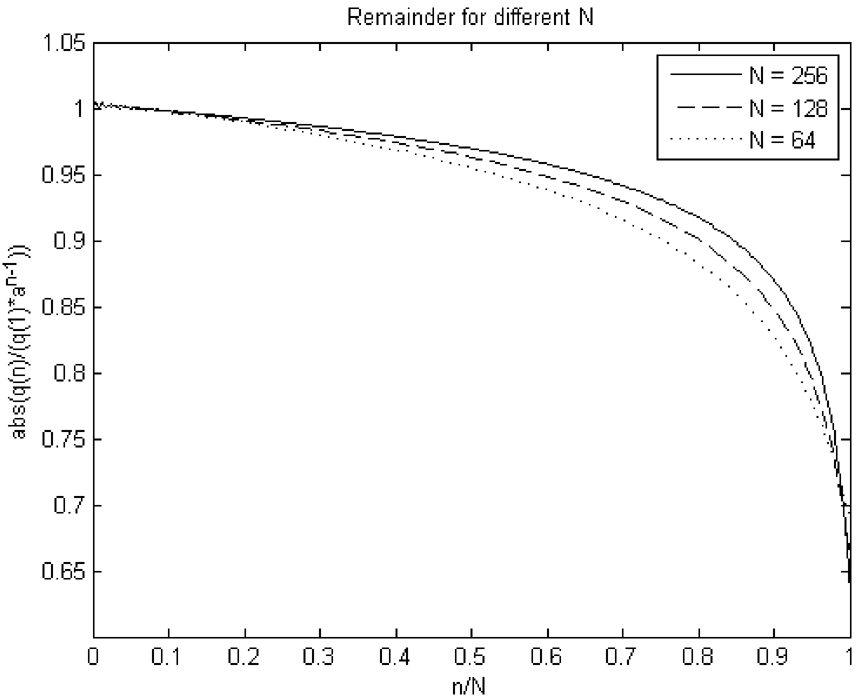

Figure 5.15 - The remainder, i.e. the left hand side of formula 4-21, for three different antenna lengths N.

The remainder, and consequently the whole field distribution, thus has a limited dependence on N that has to be taken into account. The question about how to determine the polynomial coefficients remains open.

5.5 General discussion

Testing with the expression for a passive periodic structure in section 5.2 shows that it picks up the behaviour well in the middle and left part of the antenna, but there is a significant difference in the right part where the field strength either drops or raises. Also, there is a non-periodic interference phenomenon for some frequencies, which can not be observed with a unit cell analysis. Another interesting observation in this part was that some frequencies gave higher field strength than the design frequency.

The effect of the edge elements were studied by altering the length of and distance between the three outermost elements at each side of the antenna. One could have hoped that these design changes would result in a more even field distribution, i. e. straighten the bend a little, but there was not much difference in that case. What could be observed, though, was a reduced magnitude of the inter-cell variations shown when taking multiple measuring points in each unit cell.

In section 5.3 the propagation constant was given closer attention by studying the convergence of the Z transform of the simulated values. No definite convergence limit could be identified, and different ways of choosing a limit all resulted in an interval containing $|z| = 1$ meaning that the imaginary part could be zero. Thus, the hypothesis that the propagation constant is real could not be falsified.

To handle the bend, a model where a polynomial is multiplied with the exponential used for passive periodic structures was proposed and tested for the design frequency. For the default setup with 256 antennas and three values removed on each side there was still some remaining effects not picked up. Removing more values gave a better match between the simulation and the model, and for about 30 removed values a polynomial of degree three the deviation is of at worst 0.7 %. This is still a quite large deviation, and the better fit on the bend had a trade-off in worse fit at the left part of the antenna. The coefficients showed to depend on both the frequency and the antenna length, but no method to determine them in advance was proposed. Also, the whole field distribution has a dependence of the number of elements in the array, which could be seen when comparing normalised values for different antenna lengths.

6

6 Conclusions and future work

In this thesis, the electrical field above a Hansen-Woodyard endfire antenna consisting of monopoles over a perfectly conducting ground plane has been studied. The difference from earlier studies is that the structure in this case is active, with feed in every element. The aim has been to investigate whether it can be considered a periodic structure, analysed using a representative unit cell, as is the case for a passive periodic structure.

First of all it was concluded that there indeed is a coupling between the elements that can not be neglected. The theory for a passive periodic structure applies sufficiently well on the left part of the antenna, but there is a significant difference in the right. Trying to pick up this behaviour using a polynomial gives a better fit where the electric field curve bends off, but worse where the fit was good applying the passive periodic structure formula. The propagation constant and whether it is real or not has to be analysed using a different method than was done in this thesis.

The antenna is periodic enough to be analysed using a unit cell, but the accuracy is not so good, and more work is needed in order to get a better model. Not all of the observed phenomena could have been observed using analysis in a unit cell; one example is the interfering frequencies, and another the overall dependence on the number of elements. These are phenomena that may be interesting to analyse from a design perspective, for example by changing the phase difference or letting the outermost elements be parasitic. The effect of the edge elements are another area to dig deeper into in future work.

References

[1] Bansal. R, "*Fundamentals of Engineering Electromagnetics*", Chapter 8, Taylor& Francis Group, LLC, 2006.

[2] Pozar, D. M., "*Microwave Engineering*", Fourth edition, John Wiley& Sons, 2011.

[3] Ericsson, A., "*Self-Supported Hat Feed Reflector Antenna for SATCOM Applications*", Department of Electrical and Information Technology, Lund university, 2013.

[4] IEEE Standards Board, "*IEEE Standard Definitions of Terms for Antennas*", The Institute of Electrical and Electronics Engineers, Inc., 1993.

[5] Volakis, DR.J. L, "*Antenna Engineering Handbook*", Fourth edition, The McGraw-Hill Companies, 2007.

[6] Orfanidis, S. J., "*Electromagnetic Waves and Antennas*", 1st ed., Sophocles J. Orfanidis, 2008.

[7] Jin, J.-M., "*Theory and Computation of Electromagnetic Fields*", 1st ed., John Wiley & Sons, Inc., 2010.

[8] Balanis C.A, "*Modern Antenna Handbook*", Ch 29, Wiley& Sons, Inc., 2008.

[9] Lane. Z, "*Antenna Technology*", Ch 1, First Edition, Research World ,2012.

[10] Balanis C.A, "*Antenna Theory, Analysis and design*", Third edition, John Wiley& Sons, 2005.

[11] Bahadori, H., Alaeian H., and Faraji-Dana R., "*Computation of periodic Green's functions in layered media using complex images technique*", Progress In Electromagnetics Research, Vol.112, 225-240, 2011.

[12] Gibson, W. C., "*The method of moments in electromagnetics*", First edition. Taylor& Francis Group, LLC, 2008.

[13] Burke, GJ and Pogio, AJ, "*Numerical Electromagnetics code (NEC) Method of Moments, Part I: Program description - Theory*", Naval Ocean Systems Center, San Diego, 1981, compiled by Adams, C., 2007, collected from http://users.commspeed.net/k7qo/NECpart1.pdf, 2013-07-25.

[14] Collin, R.E, "*Field Theory of guided waves*", second edition, Wiley interscience, 1990.

[15] Elachi, C., "*Waves in Active and passive periodic structures: A Review*", Proceedings of the IEEE, Vol. 64, Issue 12, December 1976.

[16] Itoh, T., "*Periodic Structures for Microwave Engineering*", Department of Electrical Engineering, University of California, 2005.

[17] Bienkowski, P. and Trzaska, H., "*Electromagnetic measurement in the near field*", second edition, SciTech Publishing, Inc., 2012.

[18] Valerio, G., Baccarelli, P., Burghignoli, P., and Galli, A., "*3-D Green's function in 1-D periodic structures: A comparative analysis of the acceleration techniques*", Electronic Engineer Department, University of Rome, 2006.

[19] Burke, G.J. and Pogio, A.J., "*Numerical Electromagnetics code (NEC) Method of Moments, Part III: NEC User's Guide*", Naval Ocean Systems Center, San Diego, 1981, compiled by Adams, C., 2007, collected from http://users.commspeed.net/k7qo/NECpart3.pdf, 2013-07-25.

[20] Spanne, S., "*System och Transformer I - Tidsdiskreta lineära system och komplex analys*", Matematiska Institutionen, Lunds Tekniska Högskola, 2006.

[21] Kopp, C., "*Wedgetail AEW&C Aperatures*", Air Power Australia Technical Report APA-TR-2011-0301, 26th March 2011, collected from http://www.ausairpower.net/APA-Wedgetail-Antennas.html, 2013-07-25.

[22] Kopp, C., "*Wedgetail - Australia's "Pocket AWACS"*", 1999, collected from http://www.ausairpower.net/TE-Wedgetail-99.html, 2013-07-25.

[23] Munk, B. A., "*Finite Antenna Arrays and FFS*", Wiley-Interscience, 2003.

[24] Kittel, C., "*Introduction to Solid State Physics*", 8st ed, John Wiley & Sons, 2005.

[25] Holter, H. and Steyskal, H., "*On the Size Requirement for Finite Phased-Array Models*", IEEE Transactions on Antennas and Propagation, Vol. 50, No. 6, June 2002.

[26] Hansen, W. W. and Woodyard, J. R., "*A new principle in directional antenna design*", Proceedings of the Institute of Radio Engineers, Vol. 26, No. 3, March 1938

[27] Saleh, B. A. E. and Teich, M.C., "*Fundamentals of Photonics*", second edition, Wiley Interscience, 2007

[28] Munk, B. A., "*Frequency Selective Surfaces*", John Wiley & Sons, Inc., 2000